

Fig. 31: Types and interpolation strategies for the interrogation subgrids. The three selected subgrid types are described in the text. Red lines show the shapes of the subgrids. The black rectangles at subgrid boundaries represent the constant or average values of displacement, while the blue ellipses correspond to subgrid boundary nodes with individual displacement in both directions.

3.5.2 Adaptive subgrids

We developed three types of numerical subgrids that were locked on the central parts of the evolving folds (target areas) (Fig. 31): 1. **isovolumic subgrid** with a constant factor of displacement ($k\Delta X$) of all boundary elements (Fig. 31.1, 2. **non-isovolumic adaptive and polygonal subgrid** with individual displacement (ΔX) of all boundary elements (Fig. 31.2), and 3. **rectangular non-isovolumic adaptive subgrid**, where the displacement of boundaries is prescribed by average displacement ($a\Delta X$) of all boundary elements (Fig. 31.3).

For the **isovolumic subgrid** (Fig. 31.1), it was difficult to hold the subgrid on the central part of the target area (axial part of the fold). The application of the **non-isovolumic and polygonal adaptive subgrid** was finally rejected due to the numerical diffusivity problems that become more significant for complex geometries with sharp gradients in the relative motion of elements. In other words, the real perturbation of the interface between the rheologically contrasting domains shows a shorter wavelength than the displacement field grid, resulting in artificial distortion of the subgrid boundaries. Finally, the **rectangular non-isovolumic adaptive subgrid** proved as a fair compromise between the first two subgrid setting options. This subgrid remained centred on the domains of target areas during the progressive evolution of the displacement field. In addition, for two neighbouring target areas, individual boundaries remained parallel without any artificial development of gaps or overlaps.

3.5.3 Divergence in adaptive subgrids and mass balance

To trace the melt flow related mass balance in the developing detachment folds, we used two neighbouring cells of subgrids (*rectangular non-isovolumic adaptive subgrid*), where the first cell overlaps with the evolving fold structure and the second one confines the melt source area beneath that fold. For both subcells, we calculated the average values of divergence of the velocity field from all subcell nodal values and across all the time frames that capture the fold development. This allows to trace the time evolution of average divergence and study the relative mass balance between the amplifying fold and the melt source beneath the fold. We studied the time evolution of divergence for the target areas (Cell 1 and Cell 2; Fig. 32a) and compared the trends in this evolution with their modal amount of melt. The divergence/modal content vs. time diagrams reveal four distinct stages associated with fold development. In the fold structure (Cell 1), the average divergence decreases (minimum values), which is associated with the inflow of the weak wax and wax melt. At the same time, the average divergence increases in the source area (Cell 2) up to maximum values, which is coupled with melt outflow (Fig. 32b). Progressive amplification of the studied fold is associated with an increase of divergence up to zero, which coincides with the inflection point of the divergence/time curve for the studied fold (Fold 3). Subsequently, the source area (Cell 2) shows a decrease of divergence, which is attributed to the continuous loss of material that flows upwards into the fold area (Cell 1). The third stage in the fold development and associated mass transfer is marked by a further increase in divergence up to maximum values. This is linked with the increasing contribution of the extension in the sand layer and the wax in the hinge sector of the locked up folds. During this stage, the vertical limbs of the locked folds undergo attenuation and can be pinched by the surrounding sand, which results in the formation of diapirically shaped folds (Fig. 32c). This is complementary with decreasing positive divergence in the source domain (Cell 2), linked with a decreasing rate of melt outflow into the overlying region (Cell1).

The sum of the melt amount quantified in both subdomains (in folded and source areas) remains nearly equal for the incriminated timesteps and corresponding average divergence reveals opposite trends in both studied subdomains. This equilibrium serves well as an approximate test of mass conservation in the studied system.

We studied the mass balance for corresponding subdomains in all the sequential folds in the model domain (Fig. 33). The size of individual Cells is implicitly taken into account by calculation of average divergence in target areas. Although for the analytical solution, it is also possible to weight the integral divergence by the areal size of the current subgrid area, in this study, we calculated only the discrete (point) values of divergence for further analysis.

For folded areas, the range of divergence values comprising the maximum, inflection, minimum and finite point of the divergence evolution curve, respectively, progressively decreases in the sequence of melt-cored detachment folds (F1b, F3, F4, F5, F6; Fig. 26c, 33). A similar trend is also visible for the source area subdomains,

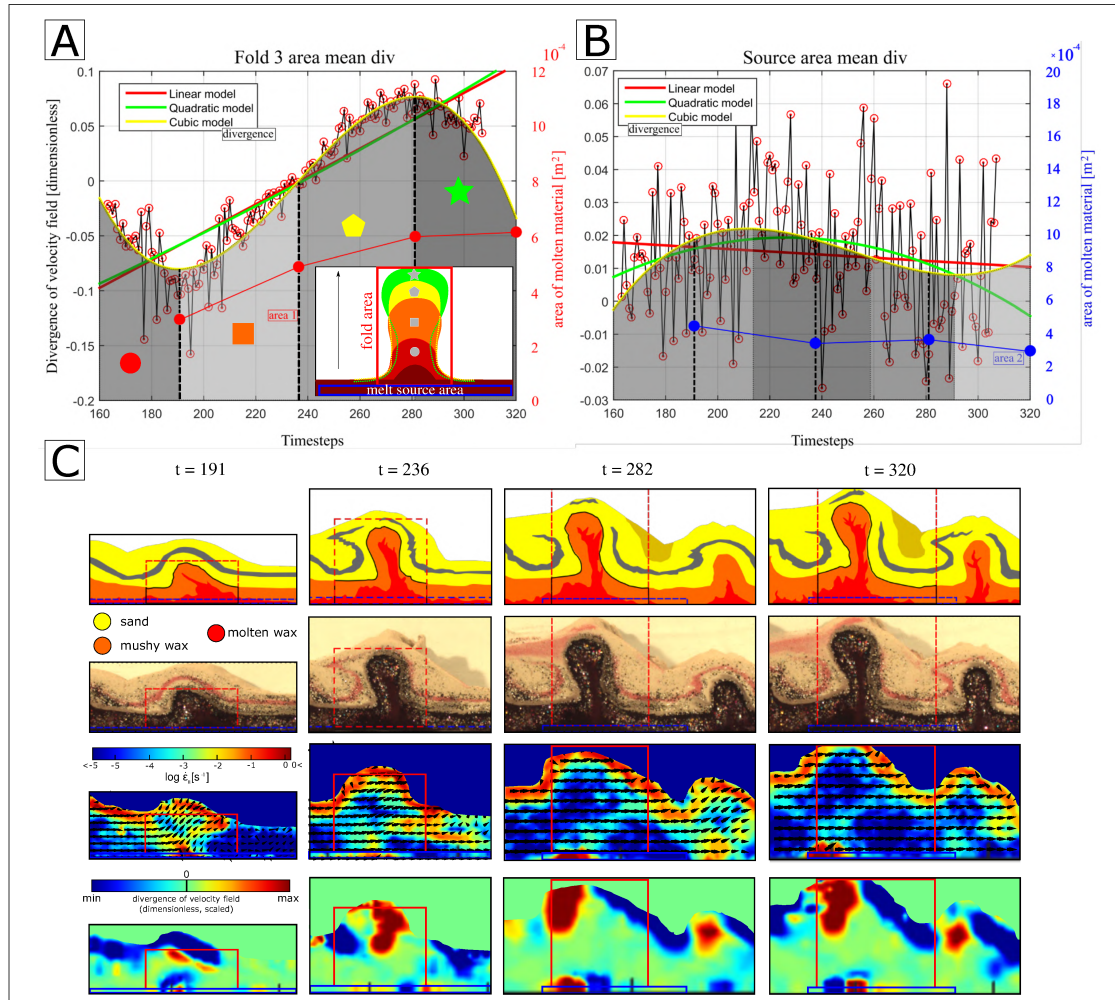


Fig. 32: Evolution of the divergence and melt content in the two traced subdomains in the detachment fold experiments (the fold and the source area) for the fold F3 (see Fig. 26c). Diagram A displays the average divergence evolution in the fold area. Key segments of the cubic interpolation curve (minimum, inflection, maximum, finite state) are also marked by the modal amount of the melt that was measured (red line with full red circles). Individual colored symbols correspond to the subsequent amplification stages of the fold as schematically illustrated in the inset. Diagram B displays the corresponding evolution of the divergence and the melt content in the source area. The blue line and blue circles show the melt amount content at specific time steps that correspond to the amplification stages (shown in inset of panel A). Panel C displays the redrawn shapes of the distorted layers, markers and the extent of remobilized melt in the fold cores, corresponding images and associated field contour-maps (divergence and shear strain-rate) for the individual amplification stages.

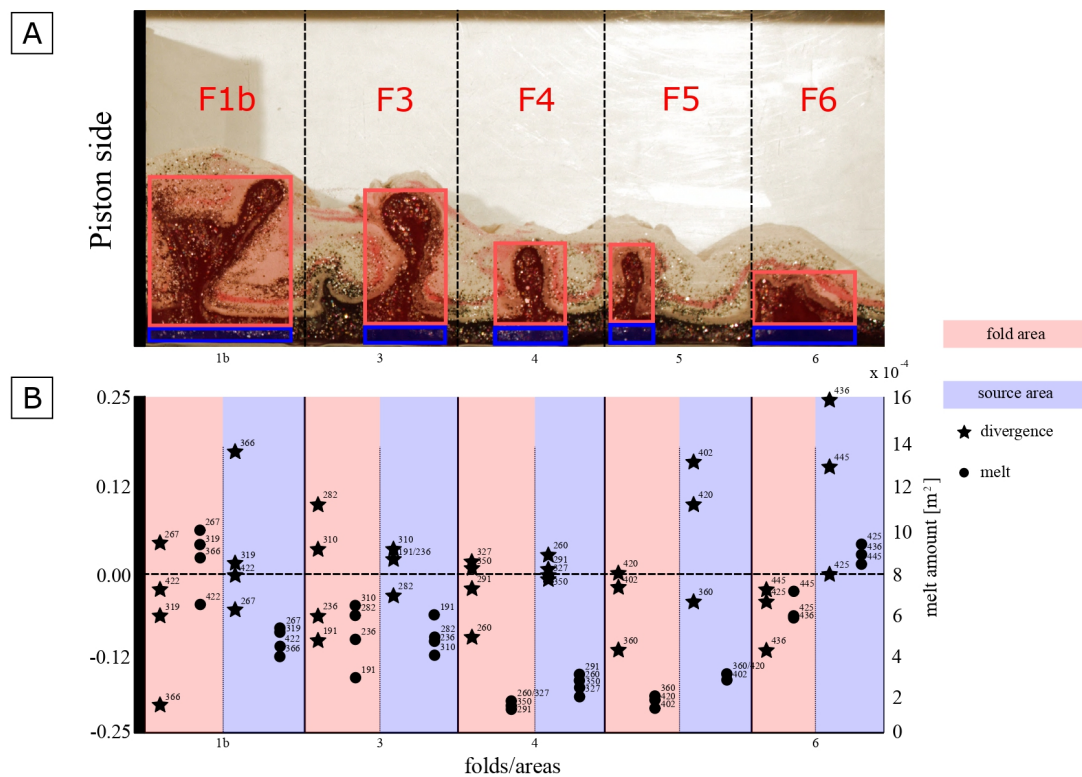


Fig. 33: Overview of the calculated divergence and measured melt amount for individual folds in the model domain. Red and blue rectangles schematically show positions and size of adaptive subgrids where divergence was calculated (fold and melt source areas). Lower panel compares the calculated mean divergence values and corresponding melt amount in significant fold evolution stages.

except for fold 5 and 6. The melt content values in associated stages partly follow this trend, except for fold 6.

The maximum values of average divergence decrease from fold 3 to fold 6 while in source areas, they reach the highest values for folds 1b and 6, situated at the edges of the model. The latter folds (1b and 6, Fig. 26c) also contain a significantly higher amount of melt in fold cores and source areas.

The minimum value of average divergence is characteristic for fold 1b and progressively increases with increasing distance from the indenter. A similar trend is also visible in respective source areas.

Generally, the time-steps with maximum average divergence in individual folds correspond to time-steps with minimum average divergence in their respective source areas. This opposite trend of evolution curves of average divergence represents clear evidence for mass conservation in neighbouring “melt source” and “fold core” subdomains.

3.6 Discussion

The two types of presented experiments illustrate complex lithospheric domains, where crustal scale transfers are controlled by the implemented stratification that induces mechanical anisotropy and promotes folding. The major aim of the present work was to illustrate the correlation of the deformation features with the variation of the velocity and strain-related parameters derived from the displacement field using the PIV technique, in order to explain the associated kinematic framework and relative mass redistribution on a local scale. We discuss briefly some of the geodynamic implications of the described models. Further detailed analysis of these models will be presented in separate studies.

3.6.1 Interpretation and significance of the calculated parameters in the oroclinal buckling models

Variations of all calculated parameters were neglected close to the margins of the model domains with anticipated edge effects at solid walls. The magnitude of the displacement field clearly reveals that the interface between the two subdomains is marked by contrasting element velocity in both models (Figs. 25a,b,c; 29a,b,c). This velocity gradient demarcates the deformation front with strong deformation localization. All parameters derived from the displacement field are well correlated with major deformation features developed exclusively at the surface of the oroclinal model domain. For example, the divergence of the velocity field map (Fig. 25d,e,f) indicates the convergent zones together with all the extensional zones. The divergence is rarely employed for the analysis of the displacement field (e.g. Kettermann et al., 2016, Reiter et al., 2011). Instead, the authors usually plot the horizontal and vertical components of strain (e.g. Adam et al., 2005; Krézsek et al., 2007; Boutelier and Oncken, 2011; Warsitzka et al., 2013). We suggest that the divergence represents a valuable parameter that reflects volumetric deformation and mass balance in the evaluated model domains.

In the oroclinal buckling models (Fig. 25), all negative values of divergence (convergent zones) are concentrated in elongated areas bound by thrust zones, while areas with positive divergence show extension, e.g. in crestal parts of upright folds, collapsing thrust belts or pop-up structures (Fig. 34, 35a). Formation of the thrusts, pop-up belts and elevated plateaus is primarily driven by mechanical coupling between the lower silicon layers and upper sand layer (Fig. 34c). Volumetric changes, associated with non-zero values of the divergence of the velocity field, inside and alongside the oroclinal, are then directly linked with internal deformation of the sand layer, e.g. marked by thrusting in front of the laterally propagating oroclinal hinges (Fig. 35a).

The second invariant of the deviatoric part of the strain-rate tensor (Fig. 25g,h,i) serves well for mapping of areas that are related with variations in the shear-strain component without the volume changes, independently to the referential frame. The

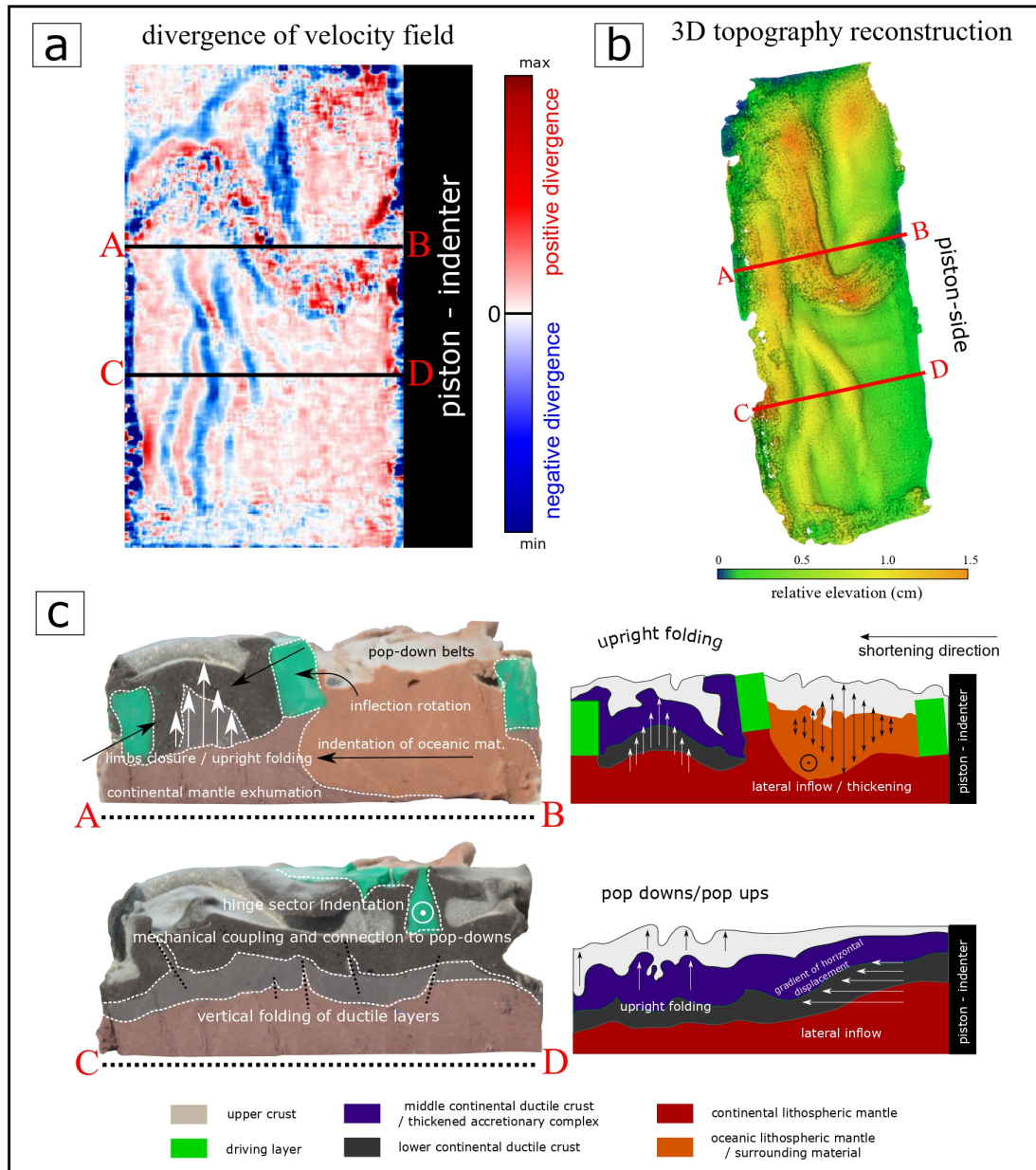


Fig. 34: Development of topography and a mechanical coupling between the upper crust and lower lithosphere in the model of oroclinal buckling. Panel A displays a contour map of the velocity divergence (after Fig. 25). The finite topography of the model surface (panel B) is represented by the DEM (digital elevation model), calculated by MicMac software (e.g. Galland et al., 2016). Sections A-B and C-D in panel C reveal the material transfer in the center of the model domain. Section A-B displays deformation of middle-lower crust and upper mantle segment between the orocline limbs, while section C-D displays development of pop-up and pop-down structures in the middle part of the model domain. Cross-sections of the model show the distorted silicone layers without the topmost sand layer (removed before the model slicing). Interpretative diagrams show the general deformation pattern that includes the sand layer.

zones of maximum shear strain values correlate primarily with the concentrated deformation along the rheological boundaries in the models and also reflect the development of major fault zones. We suggest that the total amount of shear strain with respect to the strain/-rate tensor is most conveniently expressed by the second invariant of its deviatoric part (equation 3.5) than simply by a single shear component (e.g. e_{xy}). In the vorticity of the velocity field (Fig. 25j,k,l), the most remarkable feature is seen in the rotation of the individual fold limbs around the inflection point of the orocline. It should be taken into account that the local tendency of the rotation is not related to the spinning movement of individual domain particles, but clusters of neighbouring particles.

The most of the deformation patterns in the upper crust are related to upright folding of lower ductile layers (Fig. 34c, section C-D) in both orocline hinge sectors. Subdomains of positive or negative divergence (Fig. 34a) can be correlated with the folded topography of the DEM (digital elevation model)(Fig. 34b). The upright folding and formation of pop-ups between the orocline limbs is supported by orocline amplification (Fig. 34c, section A-B). The pop-up and pop-down lines are curved and reveal a tendency to converge at the orocline inflection point. This pattern is also well shown in the vorticity field (Fig. 25A,j-l), where the rotational potential of the surface material around the inflection is obvious. The development of the finite topography pattern is associated with: 1. mechanical coupling between lower ductile layers and upper brittle material (e.g. Brun, 2002) and 2. amplification of the orocline, which is related with the rotational movement of the surrounding material.

3.6.2 Interpretation and significance of the calculated parameters in models of the detachment folding

The model parameters that were used for investigation of material transfer in the detachment folding models (Fig. 29) are the same as for the oroclinal buckling models. Here, the relevance of individual parameters interpretation is limited mostly by the distortion against the immobile background, as discussed above. The divergence of the velocity field (Fig. 29d,e,f) well correlates not only with sectors of extension or compression in the individual fold bodies but also with zones of melt ascent from the melt source layer. The triangular domains at the base of the folds (Fig. 29 (6),(10)) are clearly associated with melt coalescence from the source layer and later injection upwards along the axial planes of developing folds (Lehmann et al., 2017). While the inflow and vertical extrusion in mushy wax and wax melt are linked with negative anomalies of divergence, the neighbouring anomaly of positive divergence is attributed to the outflow of the melt from the melt source layer to the foreland part of the fold. The wax melt flow in the intrusion channel is then indicated by lower intensity negative anomalies that contribute to the negative part of the average divergence evolution curve (Fig. 32a).

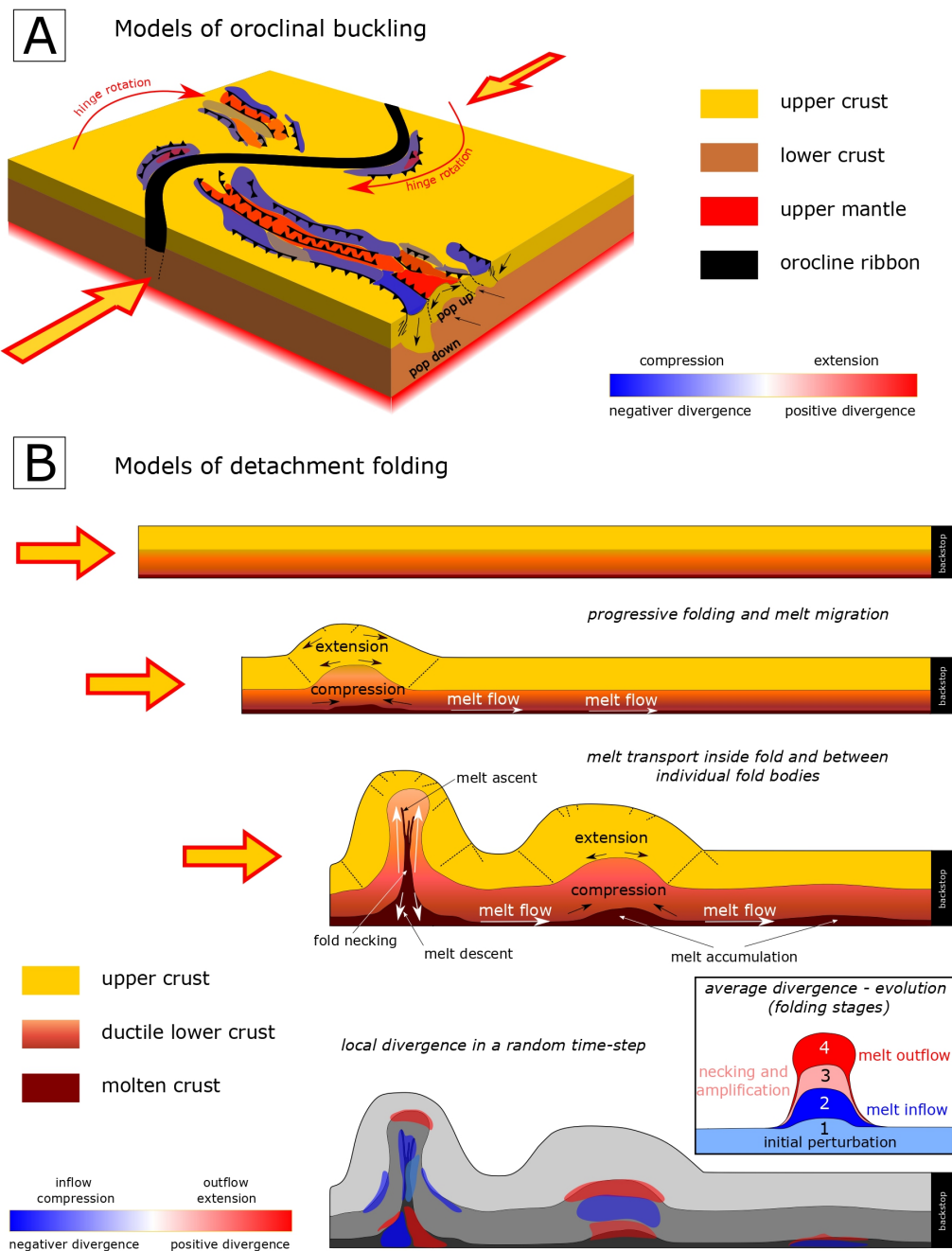


Fig. 35: The visualization of the main deformation features and material transport patterns in models of oroclinal buckling and detachment folding. Models of oroclinal buckling (A) reveal that the local positive and negative variations in divergence of the velocity field are associated with development of the pop-ups (positive values) and pop-downs (negative values). Models of detachment folding (B) show the inner transport alongside the axial plane of current fold and progressive migration of the molten material in the source layer towards the less amplified fold bodies in the frontal part of the accretionary system. Individual evolutionary stages of the detachment folds are complemented by a color pattern and a non-scaled color coding bar that corresponds to a relative range of average values of the divergence (small panel at lower-right part of (B)). All divergence polygons are only schematic (for real values see figures 25, 29 and 34).

As we discussed above, the shear strain component (Fig. 29g,h,i) is well expressed by scalar values of the second invariant (equation 3.5). Shear deformation corresponds with both the fore-thrusts and back-thrusts and also with the interface between the wax and the surrounding sand in the top part of the Y shaped fold (Fig. 29, features (8,9)). These shear zones are also reflected in both, the clockwise and counterclockwise domains in the vorticity field (Fig. 29, features (12, 13)).

3.6.3 Melt flow and mass balance in the sequence of detachment folds

The calculated average divergence of the velocity field for all individual folds (F1b-F6) in the time-plot and its correlation with the modal amount of melt in the areas of interest (melt source area in the basal layer below the fold and the folded area, Fig. 32), revealed progressively changing fold growth and associated melt flow dynamics in the sequence of developed detachment folds (Fig. 33).

The inner dynamics of the folds and the related divergence are characterized by several evolutionary stages (paragraph 3.5.3, Fig. 32a) that reflect initial perturbation, amplification and vertical extrusion of the fold body by attenuation of the verticalized limbs. The transition between these stages corresponds to the minimum, inflection and maximum (or maximum plateau), which can be followed by a slight drop in divergence during the final stages of the fold evolution. The distance between these evolutionary stages defines the magnitude of divergence scatter in the fold/source areas (Fig. 33, distance between black stars).

The maximum divergence scatter is characteristic for folds F1b, F3 and F6 that are situated close to the indenter and backstop regions and where also a higher amount of the melt was accumulated (Fig. 33, black circles).

The amplification associated with melt inflow in fold F3 was followed by the expulsion of some of that melt back into the melt source layer during the limb attenuation (Fig. 26d), which may be also reflected in the drop of the divergence values for the fold area (Fig. 33b). Simultaneously, as the folds lock up, the residual melt in the source layer flows laterally to the undeformed part of the model due to a pressure gradient driven by the load of the thickened portion of the model (Beaumont et al., 2001; Beaumont et al., 2004; Jamieson et al., 2004; Beaumont et al., 2006; Gemmer et al., 2004; Albertz et al., 2010). This mobile melt thus thickens the detachment layer in the foreland (the melt source layer) and further assists decoupling of the overlying sequence and development of the sequential folds. This is clearly manifested by a large amount of melt trapped in the last fold of the fold array (Fig. 26c, 27c).

Small amplitude, low rate of melt transfer and low melt content in folds F4 and F5 in the middle part of the domain can be explained by 1) the difference in the thermal gradient - the lower thermal gradient in the centre of the model domain may be responsible for slightly softer wax with small buckling wavelength, 2) melt that was retained in the melt source region of fold F3 due to late stage uplift of the left

part of the fold (Fig. 26c,d), and 3) the short time interval for their growth with respect to the folds F1b and F3.

3.6.4 Application of modelling results to accretionary orogens with partially molten lower crust

Results of the detachment folding experiments presented in this study follow up on our earlier analogue modelling results that helped to identify detachment folding as a new mechanism for vertical extrusion of lower crustal rocks in accretionary orogens (Lehmann et al., 2017). A simple kinematic model of melt cored detachment folds presented by Lehmann et al., (2017) implies dynamic changes of the pressure gradients during the growth and lock up stage of these folds. In the first stage, “rapid fold amplification” is marked with an influx of melt driven by underpressure developed below the crestal domain of the fold, and associated with upright folding of the high-temperature flat layering. In the next stage, as the limbs of the fold rotated by 60°, the fold passes to “post-buckle flattening”, marked by overpressurization of the melt in the fold core that may result in the failure of the ductile walls and expulsion of the melt from the core zone along the axial plane of the fold.

Similar melt transfer dynamics can be identified in the individual folds from the detailed analysis of the displacement field in a static window that passes through the mushy wax layer of a developing fold (Fig. 30) and the analysis of the developing fold in contact with the adjacent melt source domain using the subgrid areas (Fig. 32, 33). We suggest that some of the overpressured melt locked in the core zones of the folds may be evacuated back to the source layer (Fig. 35b). This melt can be transferred along the basal layer towards the foreland due to the gravity driven pressure gradient controlled by the crustal thickening in the wedge. Finally, this melt can become soaked up into the core zone of the subsequent fold in the fold array. In nature, such a scenario would imply significant magma assimilation and differentiation by percolation through different crustal levels back and forth vertically, and sideways in the source anatexic region.

The detailed analysis of displacement field in the present study allows comparison of the melt flux rates and relative melt flow directions, which is not yet possible in the crustal scale numerical models due to their low resolution and high viscosity/velocity gradients associated with the melt channels. Our results imply that the initial wavelength and thus the maximum height of the detachment folds are likely proportional to the amount of melt available in the imminent surroundings below the fold in the source layer. The early array of detachment folds can also later coalesce into branching structures cored by melt that represents weak zones prone to thrusting in the progressively thickened frontal part of the accretionary wedge (fold F1b, Fig. 29b,c). Some of the folds can also resemble diapirically shaped metamorphic core-complexes, where the surrounding sand (upper crust) in

the synclines indented the weak verticalized limbs of the folds during progressive shortening (fold F3, Fig. 26a,d, Fig. 35b).

3.7 Conclusions

The 2D PIV approach was tested on two examples of complex orogenic models, in topographic view of the oroclinal buckling models and side view of the crustal scale detachment fold models. Our structural and dynamical analysis of the analogue models is justified by fairly accurate test results comparing the calculated and real material displacement. The model parameters, derived by the decomposition of the strain rate tensor, highlight the evolution of major deformation structures in the models and allow interpretation of the local strain fields. In addition, the adaptive subgrids extend the quantification capabilities of the displacement field on a local scale, e.g. focussing on the divergence evolution during material transfer between individual target areas (melt inflow from the source layer into the core of a progressively amplifying fold). The results of this study are further summarized as follows:

1. The accuracy tests revealed that for optimal PIV post-processing and interpretation, it is convenient to combine the regular linear grid with randomly distributed contrasting particles sprinkled on the monitored surface. The accuracy of PIV calculations is also supported by the implementation of image filtering, additional interrogation windows and the TIFF format of input images.
2. In the oroclinal buckling models, isovolumic and non-isovolumic strain components, reflect the local distortions of the sand and dominantly the vertical displacement of the sand, respectively. This vertical displacement is interlinked with the amount of mechanical coupling between the lower ductile layers and the upper brittle crust (Fig. 35a).
3. The non-isovolumic component of the strain field (divergence) in the detachment fold experiments corresponds to 1) the extensional and compressional parts of crustal-scale folds, and 2) the dynamics of the molten material migration below and into the developing detachment folds (Fig. 35b). In contrast, the isovolumic strain field component (distortion) and vorticity correspond with dominant shearing in zones situated alongside the thrusts in the brittle part of the model and along the rheological interfaces, e.g. between the wax and sand layers or inside the folded partially molten wax layer.
4. The relative material transfer between the model subdomains can be quantified by average divergence evolution in the pre-defined subgrids and compared for example with the modal volume changes of the low viscosity and highly mobile material (molten wax).

5. The orocline buckling experiments reveal that the surface distortions reflect primarily the topography development of sand a) above the folded lower ductile layers, b) in front of laterally propagating orocline hinges, and c) orocline interlimb zones that are uplifted due to lateral inflow within the lower ductile layers (lower crust and lithospheric mantle).
6. The divergence analysis of the displacement field in the detachment folding experiments revealed systematic variations in the height of the folds and their modal melt content that are related to the inflow rate of melt into their cores. The overpressurization of the melt in the locked folds leads to melt expulsion back into the melt source layer, where it can be transferred further laterally into the foreland and facilitate detachment folding of the subsequent folds.

3.8 Appendix

3.8.1 Accuracy of the calculated displacement field

The accuracy testing of the displacement field in both models is an integral part of the present study (chapter 3.3.4 and 3.4.5). These tests justify the PIVlab based calculations for further parametric study and quantitative model evaluation. Many commercial softwares (e.g. *FlowMaster from LaVision*, *DynamicStudio etc.*) have implemented self-testing procedures where relevance of the calculated displacement/velocity respective to the real element displacement is tested. The PIV lab, as a freeware alternative to those software platforms, is also equipped with a self-testing procedure. This testing procedure creates synthetic particle images where real particle displacement is compared with the corresponding displacement calculations (Thielicke and Stamhuis, 2014 or Boutelier, 2016). The aim of the testing in our study was to evaluate the appropriate setting of the number of interrogation windows, surface colour conditions, image type and filtering, and geometrical setting of the models that can affect resultant displacement field (the best settings are described in chapter 3.3.4 and 3.4.5).

In general, the testing procedures revealed that the optimal set up of the PIV calculations in our models employs the TIFF image input format, additional filtering, colour variability of the model surface and multiple interrogation windows. The post-processing of the image sequences revealed that the calculations of the displacement field can be influenced or biased by several factors that should be taken into account during preparation of the model domain, image capturing and post-processing of the images. These factors comprise the analyzed image quantity, the image format, number of interrogation windows and resolution, light conditions and artificial motions of the model domains and camera position. We provide a summary of the testing results, which could be helpful for researchers that want to use the PIV (PIVlab toolbox) analysis for similar analogue models.

Quantity of analyzed images

The post-processing procedure revealed that the TIFF format is convenient for smaller image sets that cover the entire evolution of the model domain. In contrast, the JPG format can be employed for previewing the displacement fields of large image sequences. We suggest that further testing should focus on the optimal image capture frequency to decrease the computational and data storage requirements. However, the optimal capture frequency is important to achieve a good balance between small and large displacements between successive images. The finding of convenient sampling of image set for optimization of precision in resultant displacement field is a subject of empirical work. Too small increments result in a bad signal-noise ratio, whereas too large increments can result in loss of correlations/markers. These factors are all well discussed in Thielicke (2014) and Thielicke and Stamhuis (2014).

Number of interrogation windows

Increasing the quantity and decreasing the size of interrogation windows results in higher resolution of the calculated displacement field. Although the large and dense field grids are convenient for detailed investigation of local deformation patterns, high resolution is conversely coupled with increasing number of artefacts. Sparser displacement fields do not authentically reflect real material movement on the local frame but can be employed for general development of the model dominated by homogeneous deformation. The effects related with sparse and dense displacement fields, according to numbering and sizing of interrogation windows, are discussed e.g. in Thielicke (2014)

Deformation artefacts during preparation and experimental runs

A crucial issue, negatively influencing the PIV calculated fields, arises from the changes in laboratory light conditions during the experimental runs. Slight light variations are introduced by passing by persons (or insects) or by propagation of shadows during motion of solid walls confining the model domain. Potential distortions can be also caused by the vibrations of the whole apparatus, produced e.g. by the stick-slip effect of the moving plate, the motor or by steps of passing by persons.

Image capture issues

The camera should be also conveniently positioned at a distance to cover the whole model domain with sufficient image resolution. For long rectangular domains, images should be corrected for the effect of *Petzval field curvature* (e.g. Riedl, 2001), associated with the curvature of the lens. Since the development of topography in the orocline models is associated with motions of particles in a direction towards the camera lens, the evaluated displacements in subdomains that are closer and farther

from the camera lens (deformed and non-deformed subdomains of the models, Fig. 25c) are not equivalent, but are likely negligible for small vertical topography as in the models of oroclinal buckling. It should be noted that these shifts are removable by correction techniques that are implemented in some commercial softwares (e.g. DaVis from LaVision) or potentially can be implemented in MATLAB (e.g. Boutelier, 2016) or Python environments.

3.8.2 Subgrid calculations and Marker in Cell method

The adaptive subgrid calculation is based on the same principle as the tracing of virtual markers. Every point of the subgrid is moved to a new position, where actual values of the displacement are interpolated from the surrounding nodal values. In summary, we can suggest that for the purpose of preliminary dynamic interpretations, the rectangular non-isovolumic adaptive subgrid was sufficient to reveal the relative mass balance between the domains of interest. Nevertheless, we also suggest that for reliable mass balance analysis in the subdomains, consisting of e.g. one type of material, the non-isovolumic adaptive and polygonal subgrid would be most appropriate. However, to suppress the effect of a numerical diffusion, it would be necessary to employ a second-order subgrid for local grid interpolations. This requires interpolation of new boundary positions using the displacement values not only from the surrounding nodal values but also from the equivalent grid values between the two subsequent time-steps. This approach is similar to the principle of the *Marker in Cell* technique (e.g. Gerya and Yuen, 2003).

3.8.3 Testing of the PIV resultant displacement field

For qualitative validation of the resultant displacement field acquired using the PIV, we tested different settings of the calculations and input image formats (Fig. 36). We compare processing results using both the JPG and TIFF images, colour variability of the studied surface, amount and size of the interrogation windows and optional image filtering (intensity highpass, intensity capping). The interrogation windows represent sub-samples of the images, where pixel clusters are identified and subsequently employed for cross-correlation analysis. The size and number of these sub-images corresponds to the order of cross-correlation analysis and final resolution of the calculated displacement field (Thielicke and Stamhuis, 2014). The aim of the PIV tests was to achieve the best compromise between the resolution and accuracy of the resulting displacement field, evaluated by visual comparison of the real and calculated displacement. While the real displacement is defined by movement of physical markers (an orthogonal grid of coloured sand lines or contrasting particles), the calculated displacement corresponds to the movement of virtual markers that match the original x, y positions of the pre-selected physical markers. The testing procedure consists of the following steps: 1. Attribution of virtual point markers to initial physical markers (the finite position of physical markers that represent

a surface sand grid) 2. application of a displacement to the virtual markers, 3. quadratic interpolation of the displacement in new positions of the virtual markers from the surrounding nodal values (the calculated displacement grid is sparser than the true displacement) for all time steps, and 4. imaging of the finite positions of virtual markers and their visual correlation with the position of physical markers. For all the tests, we scripted the associated procedures in MATLAB environment. The test results for the chosen PIV settings are summarized in Fig. 36. The default tested setting is marked by two embedded interrogation windows (Fig. 36e,e) and revealed relatively low degree of spatial correlation between the virtual and physical markers, irrespective to the chosen image format. The arrangement of virtual markers roughly follow the grid lines of the colored sand, but are scattered in highly distorted surface subdomains and locally form arbitrary isolated clusters, e.g. along the longitudinal linear (red) markers (Fig. 36a, 36e). Another test was performed for an experiment, where the color variability was enhanced by powdering the surface with dark sand (Fig. 36b,f). This test in general revealed a lower degree of virtual marker scattering with respect to the sand lines than for the default test. However, in several places and especially for the JPG format (Fig. 36b), the calculated solutions show high degree of scattering or completely incorrect positions (Fig. 36b,f). The third pair of tests represents the PIV analysis for three embedded interrogation windows, without additional surface powdering and applied image filtering (Fig. 36c,g). These tests resulted in a fairly good correlation of the virtual and physical markers in the central part, but increased degree of scattering close to the left boundary of the studied domain. The difference between the solutions for JPG and TIFF formats, respectively, is evident in slightly higher amount of erroneous solutions marked by isolated points for the JPG format (Fig. 36g). The last pair of tests characterizes the same PIV analysis setting, only the color variability of the surface was again enhanced by sand powdering (Fig. 36d,h). These tests resulted in the best match between the virtual and physical marker finite positions throughout the entire studied domain. There is only few clearly erroneous solutions that are again more abundant for the JPG format (Fig. 36d). For further analysis of the model, we chose the dataset from this last processed PIV calculation (Fig. 36h).

3.8.4 Rheometry of the analogue materials used in Part II and Part III

In the analogue modelling of the oroclinal buckling we used several silicone putties with various viscosities and densities according to a specified position in the model domain. The silicons which we used are modified GS1R gums from Rhone Poulenc in France (Cagnard et al., 2006). The measurement of viscosities of individual silicones before experiments (and re-measurement after a material recycling from the model after experimental procedure) was performed in a cylindrical viscometer (Reber et al., 2013) and density was calculated according to Archimédes law in high cylinder infilled by water. The scheme of concentric-cylinder viscometer (used in analogue modelling laboratory at Géoscience Rennes) is shown at Fig. 37 and

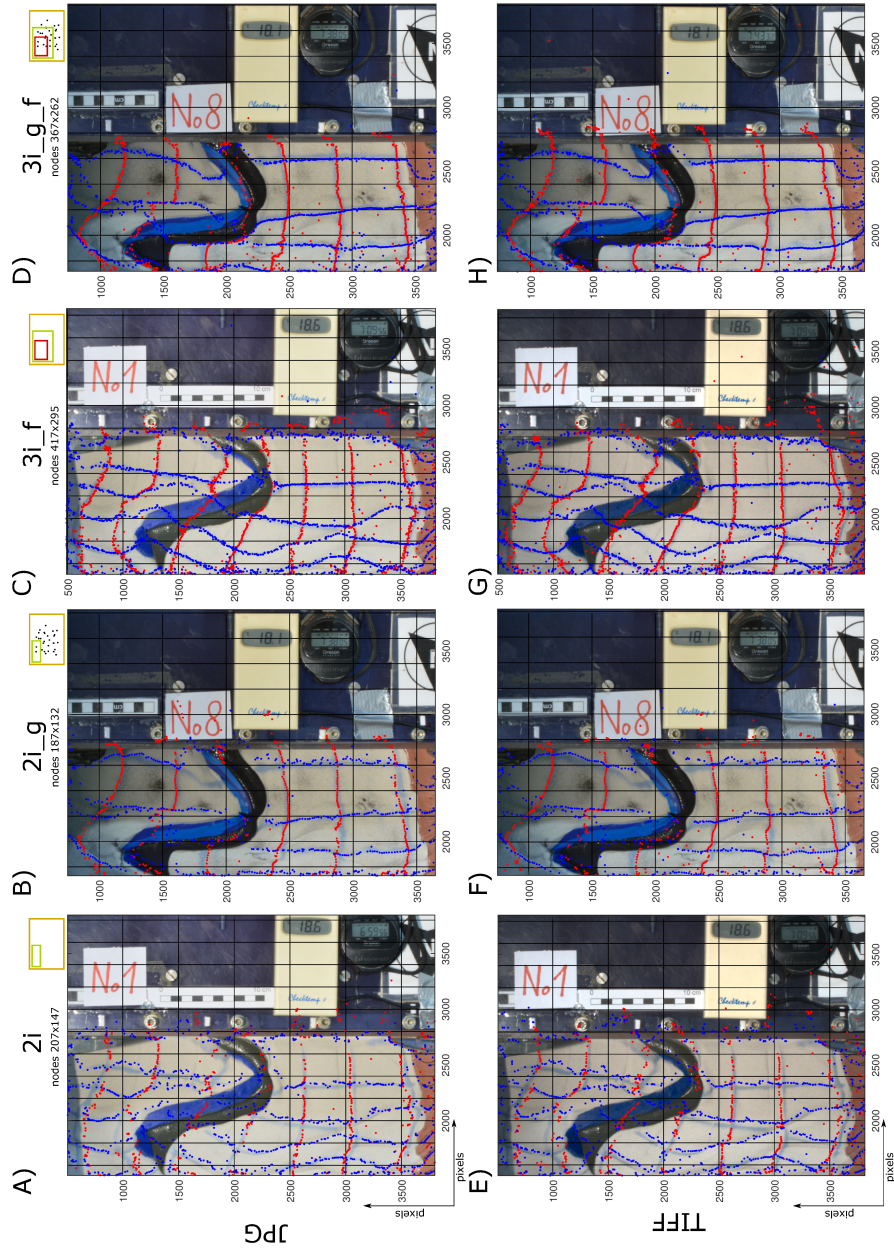


Fig. 36: Testing of the displacement field from the PIV for laboratory simulations of oroclinal buckling. Figures A-D represent the results for JPG format of input images, while figures E-H show the results with the TIFF input format. From left to the right, several PIV settings are compared; 2i - two applied interrogation windows (A,E), 2i_g - two interrogation windows and additional dark particles dispersed on the surface (B,F), 3i_f - three interrogation windows and image filtering (C,G), 3i_g_f - three interrogation windows with additional particles and image filtering (D,H)). The interrogation windows are defined by the following resolutions: 1st order: 64x64 px with step of 32 px; 2nd order: 32x32 px with step of 16 px; 3rd order: 16x16 px with step of 8 px. The blue markers originally corresponded to the lateral surface grid-lines, while red markers followed horizontal (longitudinal) direction of the grid-lines.

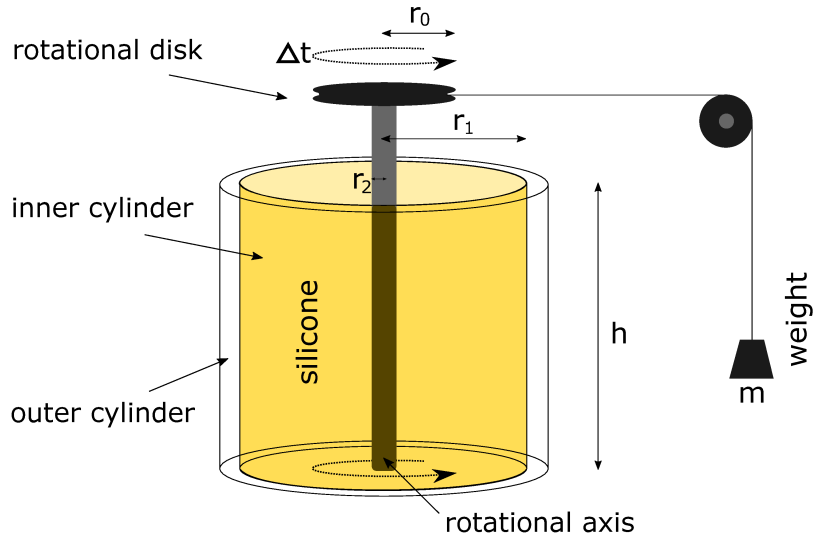


Fig. 37: Scheme of the cylindrical viscometer. The height of the cylinder (h) is 0.1 m, $r_0 = 0.05$ m, $r_1 = 0.05$ m, $r_2 = 0.008$ m and $m = 200$ g.

appropriate relationship for viscosity calculation corresponds to equation (3.9). The viscosity measurement was divided into several steps, such as: 1. Filling of the cylinder by silicone and waiting for the removing of air bubbles; 2. Application of a drag to the silicone which surrounds the small central axial cylinder; 3. Manual measurement (using a stopwatch) of time Δt for one rotation of the axis in the cylinder and calculation of viscosity η according to the following relation:

$$\eta = \frac{\Delta t}{2\pi n} \times \frac{m g r_0}{2\pi h} \times \frac{1}{2} \left(\frac{1}{r_2^2} - \frac{1}{r_1^2} \right). \quad (3.9)$$

Here n is the dimensionless number of rotations, r_0 is the radius of the turning wheel, r_1 is the inner radius of the outer cylinder, r_2 is the radius of the inner axial cylinder, m is the mass of the pulling weight and $h(l)$ is the height of the outer cylinder. The determination of power-law numbers for chosen tested materials is described in Reber et al. (2013) and referring Betteguay (1986).

In the models of detachment folding we used a paraffin wax as suitable analogue material for simulation of lower ductile crust. Before we designed and built cylindrical viscometer with variable thermal conditions, we used translation shear apparatus (Fig. 38) for a measurement of the shear stress in a wax samples and then calculated

viscosity directly from relation between shear stress and velocity gradient:

$$\eta = \tau \left(\frac{\partial u}{\partial z} \right)^{-1}, \quad (3.10)$$

where τ is the shear stress, $\frac{\partial u}{\partial z}$ is the shear velocity gradient of the wax flow and η is the viscosity.

The cylindrical wax samples were heated in a water bath to a specified temperature (Tab. 6-8). Due to the low wax thermal conductivity we kept an appropriate temperature of the samples during the experiments with average deviation of ~ 0.8 °C at the top and bottom surface, ~ 0.5 °C at the side surface and 0.3 °C at 1 cm depth. The shear velocities were progressively set to three different rates (Tab. 6-8). The resultant shear stresses were used for calculation of viscosities reflecting individual temperatures and shear-rates. The velocity gradients were calculated from measured displacement gradients for selected samples (Fig. 39).

The resultant viscosities (Fig. 40) show a pseudo-linear decreasing of viscosity with minimum values at 45 °C corresponding to $\sim 9 \cdot 10^5$ Pa.s (with counting of an additional tested samples is scatter of values situated between $9 \cdot 10^4$ Pa.s and $1 \cdot 10^6$ Pa.s). Between 45 °C and 47 °C is a zone of a rapid viscosity decreasing up to the melting point at ~ 51 °C. The viscosity measurements for wax with temperature in range $48 - 51$ °C were performed by rotational rheometer *VT 550 Haake* (supported by the Institute of Geophysics of the CAS in Prague). These viscosities are significantly lower than for $T < 47$ °C (Tab. 4,6-8) which is consistent with measurements of similar paraffin waxes used by Rossetti et al. (1999).

The general principle of the shear box experiments is in detail described in Mužík (2014).

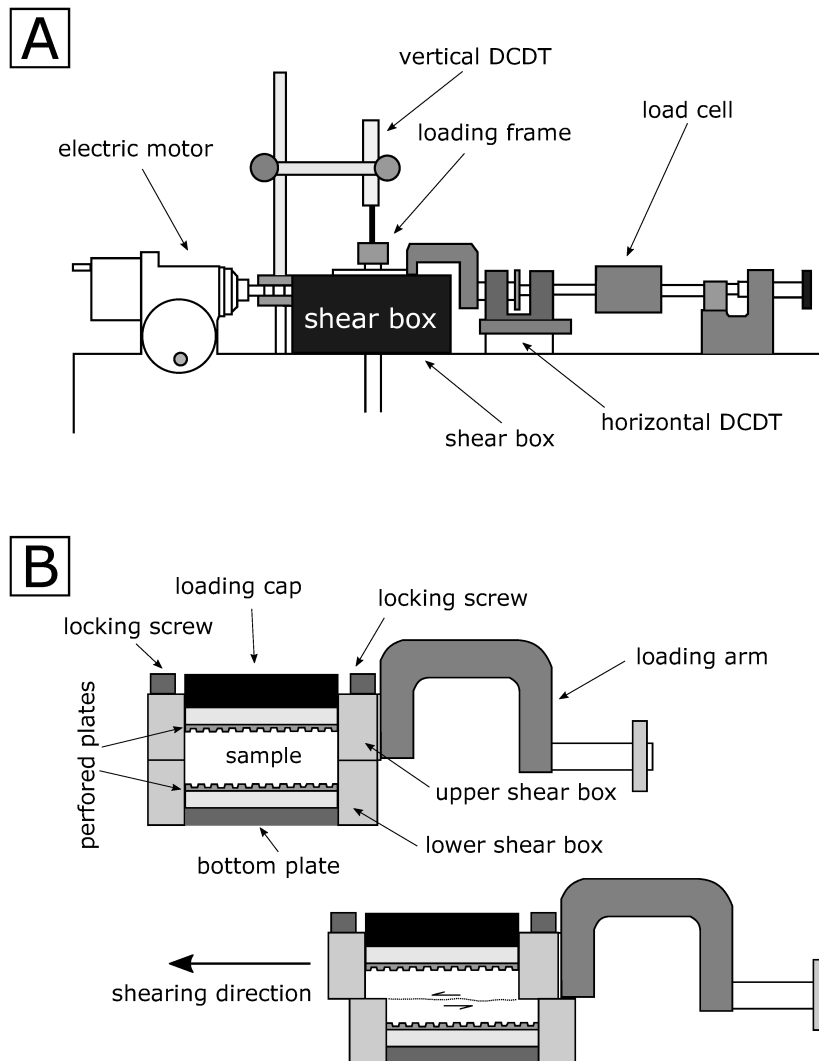


Fig. 38: Scheme of a translation shear box device. (A) lateral view to the device (developed by company *VJ Tech Ltd.* and situated at the department of Engineering Geology - Charles University) including holding frame, shear box and horizontal/vertical dynamometers (DCDT). (B) Details of the shear box core and shearing principle. Redrawn and modified after Mužík (2014).

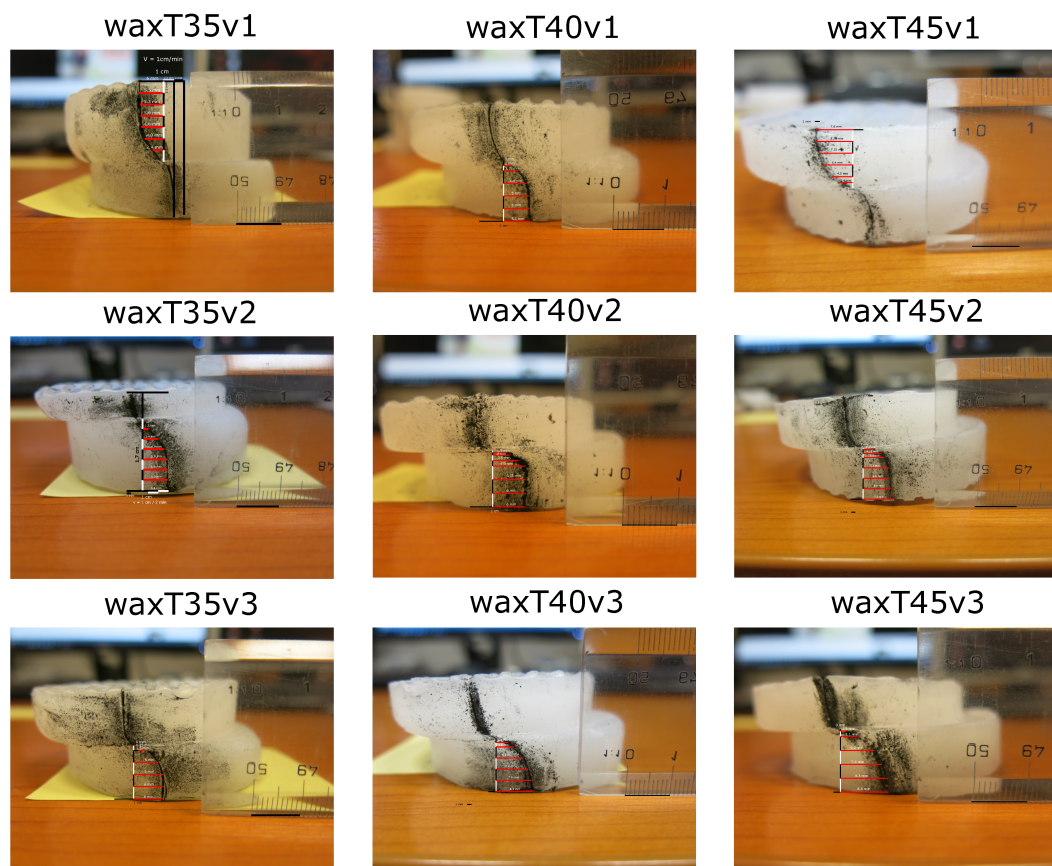


Fig. 39: Deformed wax cylinders. Selected 9 tested samples of the Paramo wax (used in modelling of the detachment folding). The temperature of a current sample is marked by T in the sample name and rate of the shearing is marked by v (see text for further details). The black and red lines are auxiliary scale-lines for measurement and calculation of the displacement/velocity gradient through shear zone of the sample. The black dust on the samples is a grinded graphite which was used for mapping of the shearing.

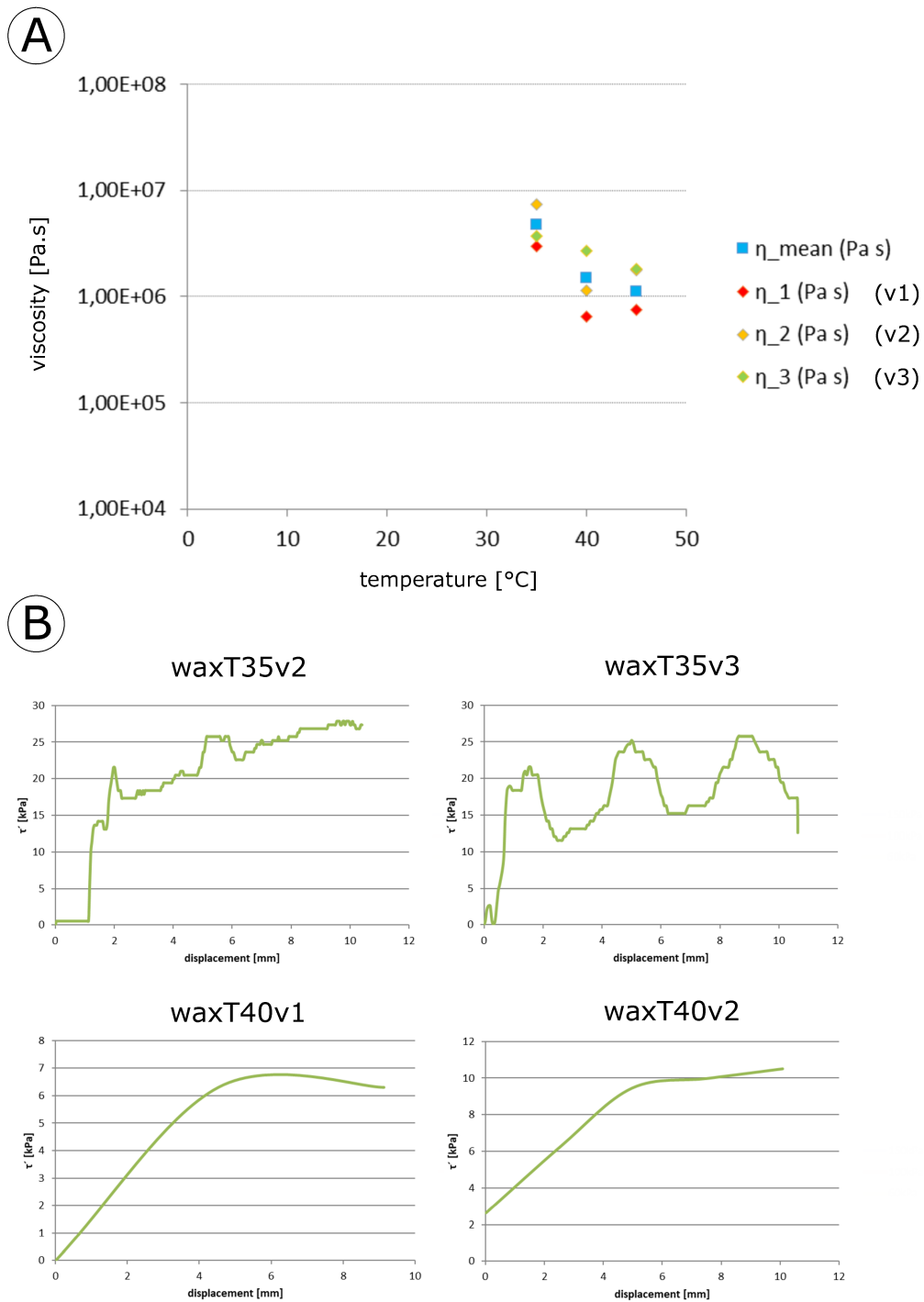


Fig. 40: Wax viscosities. Dynamic viscosities of the wax measured at the temperatures that characterize the viscosity gradient of paraffin wax in the crustal scale detachment fold experiment. Value marked with * was obtained from the shear box experiments, value marked with ** was estimated according to shearing experiments and values published in Rossetti et al. (1999). The values for temperatures > 48 °C were obtained from rotational rheometer *VT 550 Haake* (Institute of Geophysics of the CAS, Prague)

Tab. 6: Measured velocity gradient and calculated viscosity for samples with $T = 35\text{ }^{\circ}\text{C}$.

waxT35v1 1cm/1min										
u (m)	y (m)	du	dy	v (m/s)	grad v (1/s)	n	tau (Pa)	mu (Pa s)	mu (exp)	
0,006	0	-	-	-	-		7	17000	2975000	2.975E6
0,0055	0,0025	0,0005	-0,0025	8,33E-06	-0,00333333					
0,0053	0,005	0,0002	-0,0025	3,33E-06	-0,00133333					
0,005	0,0075	0,0003	-0,0025	0,000005	-0,002					
0,0046	0,01	0,0004	-0,0025	6,67E-06	-0,00266667					
0,004	0,0125	0,0006	-0,0025	0,00001	-0,004					
0,0024	0,015	0,0016	-0,0025	2,67E-05	-0,01066667					
0	0,0175	0,0024	-0,0025	0,00004	-0,016					
					-0,00571429					
waxT35v2 1cm/2min										
0,0062	0	-	-	-	-		7	22000	7451613	7.451E6
0,006	0,0025	0,0002	-0,0025	1,67E-06	-0,00066667					
0,0059	0,005	0,0001	-0,0025	8,33E-07	-0,00033333					
0,0058	0,0075	0,0001	-0,0025	8,33E-07	-0,00033333					
0,0049	0,01	0,0009	-0,0025	7,5E-06	-0,003					
0,0034	0,0125	0,0015	-0,0025	1,25E-05	-0,005					
0,0012	0,015	0,0022	-0,0025	1,83E-05	-0,00733333					
0	0,0175	0,0012	-0,0025	0,00001	-0,004					
					-0,00295238					
waxT35v3 1cm/3min										
0,006	0	-	-	-	-		6	21000	3687805	3.687E6
0,006	0,0025	0	-0,0025	0	0					
0,006	0,005	0	-0,0025	0	0					
0,005	0,0075	0,001	-0,0025	5,56E-06	-0,00222222					
0,0025	0,01	0,0025	-0,0025	1,39E-05	-0,00555556					
0,00025	0,011	0,00225	-0,001	1,25E-05	-0,0125					
0	0,0111	0,00025	-0,0001	1,39E-06	-0,01388889					
					-0,00569444					

Tab. 7: Measured velocity gradient and calculated viscosity for samples with $T = 40 \text{ }^\circ\text{C}$.

waxT40v1 1cm/1min										
u (m)	y (m)	du	dy	v (m/s)	grad v (1/s)	n	tau (Pa)	mu (Pa s)	mu (exp)	
0,0051	0	-	-	-	-		6	7000	641221,4	6.412E5
0,005	0,0025	0,0001	-0,0025	1,67E-06	-0,00066667					
0,005	0,005	0	-0,0025	0	0					
0,0044	0,0075	0,0006	-0,0025	0,00001	-0,004					
0,00315	0,01	0,00125	-0,0025	2,08E-05	-0,008333333					
0,002	0,011	0,00115	-0,001	1,92E-05	-0,01916667					
0	0,012	0,002	-0,001	3,33E-05	-0,033333333					
					-0,01091667					
waxT40v2 1cm/2min										
0,006	0	-	-	-	-		7	10000	1144414	1.144E6
0,006	0,0025	0	-0,0025	0	0					
0,00603	0,005	-3E-05	-0,0025	-2,5E-07	1E-04					
0,0049	0,0075	0,00113	-0,0025	9,42E-06	-0,00376667					
0,0035	0,0085	0,0014	-0,001	1,17E-05	-0,01166667					
0,002	0,0095	0,0015	-0,001	1,25E-05	-0,0125					
1,3	0,01	-1,298	-0,0005	-0,010817	21,63333333					
0	0,0105	1,3	-0,0005	0,010833	-21,6666667					
					-0,0087381					
waxT35v3 1cm/3min										
0,0083	0	-	-	-	-		6	14000	2671378	2.671E6
0,0078	0,0025	0,0005	-0,0025	2,78E-06	-0,001111111					
0,0072	0,005	0,0006	-0,0025	3,33E-06	-0,001333333					
0,0062	0,0075	0,001	-0,0025	5,56E-06	-0,002222222					
0,0039	0,01	0,0023	-0,0025	1,28E-05	-0,005111111					
0,0028	0,011	0,0011	-0,001	6,11E-06	-0,006111111					
0	0,012	0,0028	-0,001	1,56E-05	-0,01555556					
					-0,00524074					

Tab. 8: Measured velocity gradient and calculated viscosity for samples with $T = 45 \text{ }^\circ\text{C}$.

waxT45v1 1cm/1min										
u (m)	y (m)	du	dy	v (m/s)	grad v (1/s)	n	tau (Pa)	mu (Pa s)	mu (exp)	
0,0078	0	-	-	-	-		6	8000	494845,4	4.948E5
0,00775	0,0025	5E-05	-0,0025	8,33E-07	-0,00033333			12000		
0,00715	0,005	0,0006	-0,0025	0,00001	-0,004					
0,0064	0,0075	0,00075	-0,0025	1,25E-05	-0,005					
0,0045	0,01	0,0019	-0,0025	3,17E-05	-0,01266667					
0,0029	0,011	0,0016	-0,001	2,67E-05	-0,02666667					
0	0,012	0,0029	-0,001	4,83E-05	-0,04833333					
					-0,01616667					
waxT45v2 1cm/2min										
0,0072	0	-	-	-	-		7	6000	1507809	1.507E6
0,0069	0,0025	0,0003	-0,0025	2,5E-06	-0,001			7000		
0,0066	0,005	0,0003	-0,0025	2,5E-06	-0,001					
0,0062	0,0075	0,0004	-0,0025	3,33E-06	-0,00133333					
0,0051	0,01	0,0011	-0,0025	9,17E-06	-0,00366667					
0,00435	0,011	0,00075	-0,001	6,25E-06	-0,00625					
0,0026	0,012	0,00175	-0,001	1,46E-05	-0,01458333					
0	1,013	0,0026	-1,001	2,17E-05	-2,1645E-05					
					-0,00397928					
waxT45v3 1cm/3min										
0,0088	0	-	-	-	-		6	8000	1333333	1.333E6
0,0083	0,0025	0,0005	-0,0025	2,78E-06	-0,00111111			11000		
0,0076	0,005	0,0007	-0,0025	3,89E-06	-0,00155556					
0,0062	0,0075	0,0014	-0,0025	7,78E-06	-0,00311111					
0,0031	0,01	0,0031	-0,0025	1,72E-05	-0,00688889					
0,0011	0,011	0,002	-0,001	1,11E-05	-0,01111111					
0	0,0115	0,0011	-0,0005	6,11E-06	-0,01222222					
					-0,006					

3.9 Acknowledgements

3.9.1 Funding

This work was supported by the Czech Science Foundation grant No.: 16-17457S and the Center for Geosphere Dynamics project UNCE/SCI/006.

3.9.2 Author Contributions Statement

This research represents an integral part of the PhD project of OK. This PhD project is aimed to the analogue and numerical modelling of the material/heat transfer in large and hot orogens. All calculations in this article were provided by OK. OK performed all the oroclinal buckling models. OK and PZ cooperated on preparation of the detachment folding experiments. Primary text and figures were produced by OK and all corrections and improvements were supported by PZ. OL and OK are responsible for an idea to use the divergence theorem for investigation of mass transfer and mass balance in the model domain of the detachment folding experiments. OK performed all PIV calculations and associated scripting of routines calculating the divergence and flux balance.

3.10 References

- Adam, J., Klinkmüller, M., Schreurs, G., and Wieneke, B. (2013). Quantitative 3D strain analysis in analogue experiments simulating tectonic deformation: Integration of X-ray computed tomography and digital volume correlation techniques. *Journal of Structural Geology*, 55, 127-149.
- Adam, J., Urai, J. L., Wieneke, B., Oncken, O., Pfeiffer, K., Kukowski, N., Lohrmann, J., Hoth, S., van der Zee, W. and Schmatz, J. (2005). Shear localisation and strain distribution during tectonic faulting—New insights from granular-flow experiments and high-resolution optical image correlation techniques. *Journal of Structural Geology*, 27(2), 283-301.
- Adrian, R. J. (2005). Twenty years of particle image velocimetry. *Experiments in fluids*, 39(2), 159-169.
- Albertz, M., Beaumont, C., Shimeld, J.W., Ings, S.J., and Gradmann, S., (2010). An investigation of salt tectonic structural styles in the scotian basin, offshore atlantic canada: 1. comparison of observations with geometrically simple numerical models. *Tectonics*, 29, TC4017, doi: 10.1029/2009TC002539.
- Bajolet, F., Galeano, J., Funicello, F., Moroni, M., Negrodo, A. M., and Faccenna, C.

(2012). Continental delamination: Insights from laboratory models. *Geochemistry, Geophysics, Geosystems*, 13(2).

Beaumont, C., Nguyen M. H., Jamieson, R. A. and Ellis, S. (2006) Crustal flow modes in large hot orogens. Geological Society, London, Special Publications, 268, 91-145.

Beaumont, C., Jamieson, R. A., Nguyen, M. H., and Medvedev, S. (2004). Crustal channel flows: 1. Numerical models with applications to the tectonics of the Himalayan-Tibetan orogen. *Journal of Geophysical Research: Solid Earth*, 109(B6).

Beaumont, C., Jamieson, R. A., Nguyen, M. H., and Lee, B. (2001). Himalayan tectonics explained by extrusion of a low-viscosity crustal channel coupled to focused surface denudation. *Nature*, 414(6865), 738.

Becker, Thorsten; Kaus, Boris (2015): Numerical Modeling of Earth Systems: An introduction to computational methods with focus on solid Earth applications of continuum mechanics. figshare. Paper.

Batteguay, G. (1986). Mise au point d'une technique de viscosimetrie dun materiau analogique (silicone) utilisat en modtlisation expthimentale. Memoire de DEA, Univ. Paris XI.

Boutelier, D., and Oncken, O. (2011). 3-D thermo-mechanical laboratory modeling of plate-tectonics: modeling scheme, technique and first experiments. *Solid Earth*, 2(1), 35.

Boutelier, D. (2016). TecPIV—A MATLAB-based application for PIV-analysis of experimental tectonics. *Computers and Geosciences*, 89, 186-199.

Brun, J. P. (2002). Deformation of the continental lithosphere: Insights from brittle-ductile models. Geological Society, London, Special Publications, 200(1), 355-370.

Cagnard, F., Brun, J.-P., Gapais, D. (2006) Modes of thickening of analogue weak lithospheres. *Tectonophysics*, 421(1-2), 145–160.

Chen, Z., Schellart, W. P., Strak, V., and Duarte, J. C. (2016). Does subduction-induced mantle flow drive backarc extension?. *Earth and Planetary Science Letters*, 441, 200-210.

Collins, W. J. (2002). Hot orogens, tectonic switching, and creation of continental crust. *Geology*, 30(6), 535-538.

- Costa, A., Caricchi, L., and Bagdassarov, N. (2009). A model for the rheology of particle-bearing suspensions and partially molten rocks. *Geochemistry, Geophysics, Geosystems*, 10(3).
- Davy, P., and Cobbold, P. R. (1991). Experiments on shortening of a 4-layer model of the continental lithosphere. *Tectonophysics*, 188(1-2), 1-25.
- Duarte, J. C., Schellart, W. P., and Cruden, A. R. (2014). Rheology of petroleum–paraffin oil mixtures: applications to analogue modelling of geological processes. *Journal of Structural Geology*, 63, 1-11.
- Elsinga, G. E., Wieneke, B., Scarano, F., and Schröder, A. (2007). Tomographic 3D-PIV and applications. In *Particle image velocimetry* (pp. 103-125). Springer, Berlin, Heidelberg.
- Edel J.-B., Schulmann K., Hanžl P., Lexa O. (2014) Palaeomagnetic and structural constraints on 90° anticlockwise rotation in SW Mongolia during the Permo-Triassic: implications for Altaid oroclinal bending. *Journal of Asian Earth Sciences*, 94, 157–171.
- Galland, O., Bertelsen, H. S., Guldstrand, F., Girod, L., Johannessen, R. F., Bjugger, F., Burchardt, S. and Mair, K. (2016). Application of open-source photogrammetric software MicMac for monitoring surface deformation in laboratory models. *Journal of Geophysical Research: Solid Earth*, 121(4), 2852-2872.
- Gemmer, L., Ings, S.J., Medvedev, S., and Beaumont, C., (2004). Salt tectonics driven by differential sediment loading: stability analysis and finite-element experiments. *Basin Research*, 16(2), 199–218, doi: 10.1111/j.1365-2117.2004.00229.x.
- Gerya, T. (2009). *Introduction to numerical geodynamic modelling*. Cambridge University Press.
- Gerya, T. V., and Yuen, D. A. (2003). Characteristics-based marker-in-cell method with conservative finite-differences schemes for modeling geological flows with strongly variable transport properties. *Physics of the Earth and Planetary Interiors*, 140(4), 293-318.
- Giordano, D., Ardia, P., Romano, C., Dingwell, D. B., Di Muro, A., Schmidt, M. W., Mangiacapra, A. and Hess, K. U. (2009). The rheological evolution of alkaline Vesuvius magmas and comparison with alkaline series from the Phlegrean Fields, Etna, Stromboli and Teide. *Geochimica et Cosmochimica Acta*, 73(21), 6613-6630.
- Giordano, D., Russell, J. K., and Dingwell, D. B. (2008). Viscosity of magmatic

liquids: a model. *Earth and Planetary Science Letters*, 271(1-4), 123-134.

Giordano, D., Romano, C., Papale, P., and Dingwell, D. B. (2004). The viscosity of trachytes, and comparison with basalts, phonolites, and rhyolites. *Chemical Geology*, 213(1-3), 49-61.

Grujic, D. (2006). Channel flow and continental collision tectonics: an overview. Geological Society, London, Special Publications, 268(1), 25-37.

Hacker, B. R., Kelemen, P. B., and Behn, M. D. (2011). Differentiation of the continental crust by relamination. *Earth and Planetary Science Letters*, 307(3-4), 501-516.

Hori, T., and Sakakibara, J. (2004). High-speed scanning stereoscopic PIV for 3D vorticity measurement in liquids. *Measurement Science and Technology*, 15(6), 1067.

Hubbert, M. K. (1937). Theory of scale models as applied to the study of geologic structures. *Bulletin of the Geological Society of America*, 48(10), 1459-1520.

Jamieson, R. A., Beaumont, C., Medvedev, S., and Nguyen, M. H. (2004). Crustal channel flows: 2. Numerical models with implications for metamorphism in the Himalayan-Tibetan orogen. *Journal of Geophysical Research: Solid Earth*, 109(B6).

Jang, Y. I., and Lee, S. J. (2008). PIV analysis of near-wake behind a sphere at a subcritical Reynolds number. *Experiments in Fluids*, 44(6), 905-914.

Kettermann, M., von Hagke, Ch., van Gent, H. W., Grützner, Ch., and Urai, J. L. (2016). Dilatant normal faulting in jointed cohesive rocks: a physical model study. *Solid Earth*, 7(3), 843.

Kettermann, M., and Urai, J. L. (2015). Changes in structural style of normal faults due to failure mode transition: first results from excavated scale models. *Journal of Structural Geology*, 74, 105-116.

Klinkmüller, M., Schreurs, G., Rosenau, M., and Kemnitz, H. (2016). Properties of granular analogue model materials: A community wide survey. *Tectonophysics*, 684, 23-38.

Krézsek, C., Adam, J., and Grujic, D. (2007). Mechanics of fault and expulsion rollover systems developed on passive margins detached on salt: insights from analogue modelling and optical strain monitoring. Geological Society, London, Special Publications, 292(1), 103-121.

- Lehmann, J., Schulmann, K., Lexa, O., Závada, P., Štípská, P., Hasalová, P., Belyanin, G. and Corsini, M. (2017). Detachment folding of partially molten crust in accretionary orogens: A new magma-enhanced vertical mass and heat transfer mechanism. *Lithosphere*, 9(6), 889-909.
- Lehmann, J., Schulmann, K., Lexa, O., Corsini, M., Kröner, A., Štípská, P., Tomurhuu, D. and Otgonbator, D. (2010) Structural Constraints of the Evolution of the Central Asian Orogenic Belt in sw Mongolia. *American Journal of Science*, 310, 575– 628.
- Maierová, P., Schulmann, K., and Gerya, T. (2018). Relamination Styles in Collisional Orogens. *Tectonics*, 37(1), 224-250.
- Maierová, P., Lexa, O., Schulmann, K., and Štípská, P. (2014). Contrasting tectono-metamorphic evolution of orogenic lower crust in the Bohemian Massif: a numerical model. *Gondwana Research*, 25(2), 509-521.
- Menant, A., Sternai, P., Jolivet, L., Guillou-Frottier, L., and Gerya, T. (2016) 3D numerical modeling of mantle flow, crustal dynamics and magma genesis associated with slab roll-back and tearing: The eastern Mediterranean case. *Earth and Planetary Science Letters*, 442, 93-107.
- Mužík, V. (2014). Analysis of peak and critical strength of remoulded clay from Jiří mine. Master thesis, Charles University, Prague
- Nogueira, J., Lecuona, A., and Rodriguez, P. A. (1997). Data validation, false vectors correction and derived magnitudes calculation on PIV data. *Measurement Science and Technology*, 8(12), 1493.
- Okamoto, K., Nishio, S., Kobayashi, T., Saga, T., and Takehara, K. (2000). Evaluation of the 3D-PIV standard images (PIV-STD project). *Journal of Visualization*, 3(2), 115-123.
- Pastor-Galán, D., Gutiérrez-Alonso, G., Zulauf, G. and Zanella, F. (2012) Analogue modeling of lithospheric-scale orocline buckling: Constraints on the evolution of the Iberian-Armorican Arc. *Geological Society of America Bulletin*, 124, 1293-1309.
- Raffel, M., Willert, C. E., and Kompenhans, J. (2007). Particle image velocimetry: a practical guide. Springer Science and Business Media.
- Ramberg, H. (1981). The role of gravity in orogenic belts. *Geological Society, London, Special Publications*, 9(1), 125-140.

Reber, J. E., Galland, O., Cobbold, P. R., and de Veslud, C. L. C. (2013). Experimental study of sheath fold development around a weak inclusion in a mechanically layered matrix. *Tectonophysics*, 586, 130-144.

Regard, V., Faccenna, C., Martinod, J., and Bellier, O. (2005). Slab pull and indentation tectonics: insights from 3D laboratory experiments. *Physics of the Earth and Planetary Interiors*, 149(1-2), 99-113.

Reiter, K., Kukowski, N., and Ratschbacher, L. (2011). The interaction of two indenters in analogue experiments and implications for curved fold-and-thrust belts. *Earth and Planetary Science Letters*, 302(1-2), 132-146.

Riedl, M. J. (2001). *Optical design fundamentals for infrared systems* (Vol. 48). SPIE press.

Rosenbaum, G. (2014). Geodynamics of oroclinal bending: Insights from the Mediterranean. *Journal of Geodynamics*, 82, 5-15.

Rosenbaum, G. (2012). Oroclines of the southern New England orogen, eastern Australia. *Episodes*, 35(1), 187-194.

Rosenbaum, G., and Donchak, P. J. (2012). Structural evolution of the Texas Orocline, eastern Australia. *Gondwana Research*, 22(1), 279-289.

Rossetti, F., Ranalli, G., and Faccenna, C. (1999). Rheological properties of paraffin as an analogue material for viscous crustal deformation. *Journal of Structural Geology*, 21(4), 413-417.

Schellart, W. P., and Strak, V. (2016). A review of analogue modelling of geodynamic processes: Approaches, scaling, materials and quantification, with an application to subduction experiments. *Journal of Geodynamics*, 100, 7-32.

Schmatz, J., Holland, M., Giese, S., Van Der Zee, W., and Urai, J. L. (2010). Clay smear processes in mechanically layered sequences—Results of water-saturated model experiments with free top surface. *Journal of the Geological Society of India*, 75(1), 74-88.

Schulmann, K., Lexa, O., Štípská, P., Racek, M., Tajčmanová, L., Konopásek, J., Edel, J.-B., Peschler, A. and Lehmann, J. (2008). Vertical extrusion and horizontal channel flow of orogenic lower crust: key exhumation mechanisms in large hot orogens?. *Journal of metamorphic Geology*, 26(2), 273-297.

Sokoutis, D., Burg, J. P., Bonini, M., Corti, G., and Cloetingh, S. (2005).

- Lithospheric-scale structures from the perspective of analogue continental collision. *Tectonophysics*, 406(1-2), 1-15.
- Strak, V., and Schellart, W. P. (2014). Evolution of 3-D subduction-induced mantle flow around lateral slab edges in analogue models of free subduction analysed by stereoscopic particle image velocimetry technique. *Earth and Planetary Science Letters*, 403, 368-379.
- Thielicke, W. (2014). The flapping flight of birds—analysis and application. Rijksuniversiteit Groningen (Doctoral dissertation, PhD Dissertation).
- Thielicke, W., and Stamhuis, E. (2014). PIVlab—towards user-friendly, affordable and accurate digital particle image velocimetry in MATLAB. *Journal of Open Research Software*, 2(1).
- Vanderhaeghe, O. (2009). Migmatites, granites and orogeny: Flow modes of partially-molten rocks and magmas associated with melt/solid segregation in orogenic belts. *Tectonophysics*, 477(3-4), 119-134.
- Vanderhaeghe, O., Burg, J. P., and Teyssier, C. (1999). Exhumation of migmatites in two collapsed orogens: Canadian Cordillera and French Variscides. Geological Society, London, Special Publications, 154(1), 181-204.
- Warsitzka, M., Kley, J., and Kukowski, N. (2013). Salt diapirism driven by differential loading—Some insights from analogue modelling. *Tectonophysics*, 591, 83-97.
- Weijermars, R., and Schmeling, H. (1986). Scaling of Newtonian and non-Newtonian fluid dynamics without inertia for quantitative modelling of rock flow due to gravity (including the concept of rheological similarity). *Physics of the Earth and Planetary Interiors*, 43(4), 316-330.
- Westerweel, J., and Scarano, F. (2005). Universal outlier detection for PIV data. *Experiments in fluids*, 39(6), 1096-1100.
- Xiao, W., Windley, B. F., Sun, S., Li, J., Huang, B., Han, C., Yuan, C., Sun, M., and Chen, H. (2015). A tale of amalgamation of three Permo-Triassic collage systems in Central Asia: oroclines, sutures, and terminal accretion. *Annual review of earth and planetary sciences*, 43, 477-507.

4 Numerical modelling of crustal-scale Rayleigh-Taylor instabilities

4.1 Introduction

In this chapter a numerical model of crustal-scale diapirism will be described and discussed, this model is derived from the time-evolution of a Rayleigh-Taylor instability. This scenario follows recent studies that are aimed at describing crustal inversion due to the presence of a high density mafic lower crust which is underlain by a light felsic relaminant (Schulmann et al., 2009; Lexa et al., 2011; Maierová et al., 2012, 2014). The presence of the relaminant assumes one of the relamination scenarios which are described in Maierová et al. (2018): 1. Intra-crustal relamination, whereby felsic material which is originally derived from the subducted slab and relaminated into the crustal part of the overriding plate; 2. Sub-lithospheric relamination, where the delaminated felsic upper part of the subducting slab is progressively detached and relaminated underneath the overriding plate - into weak asthenospheric mantle; 3. Redistribution of the felsic material along the subduction channel with partial underlying of the lithospheric mantle. The presented numerical model is most relevant to the first two scenarios, where the buoyancy of relaminated material produces lithospheric-scale diapirism.

The first scenario assumes a weak and hot upper plate which could typically be the product of back-arc thinning, flexure and rapid heating due to higher thermal gradient during continuous subduction (Faccenna et al., 1996; Yasui et al., 2012, Jolivet et al., 2015). In this scenario the weak, low-viscosity relaminant could be transported in the form of a horizontal channel flow through the crustal segment (Beaumont et al., 2001; Jamieson et al., 2007) or be emplaced along the lower (MOHO) level of the crust (Maierová et al., 2012).

The second scenario assumes continuing subduction with a typically thin overriding plate and melt weakening at the lower lithospheric levels. The strength of the overriding plate is higher than in scenario 1. and the relaminant is distributed in deeper positions beneath the lithospheric mantle. Progressive heating and melt weakening is responsible for ascent of this material in the form of gravitationally driven vertical flow and later emplacement at the base of crustal levels. This relaminant later represents a source material for the development of HP granulitic domes (Schulmann et al., 2009; Lexa et al., 2011; Maierová et al., 2012; Schulmann et al., 2014; Maierová et al., 2016) and(/or) Mg-K magmas (Hacker et al., 2000, 2005; Maierová et al., 2016) that are typical for large accretionary systems such as e.g. Tibetan-Himalayan orogen (Chemenda et al., 2000; Hacker et al., 2011) or Variscan orogen (Massonne, 2001; Maierová et al., 2016).

In the previous part, where we discussed the development and dynamics of detachment folds related to the migration of anatectic lower crust, we followed a complex scenario which combines both above described situations. The assumption for those models was a significantly heated crust and the potential melting of the lower felsic crust at MOHO levels. In those models, under a continuous compressional regime, a sequence of fold-like dome structures were produced depending on crustal thickness and the total amount of melt in the system. The kinematics and dynamics of these structures combines the buckling and bending and is also associated with the intrusion of a various melt amount into the individual folds (domes) - depending on the position of folding in the whole compressed system (Krýza et al., 2019). This model is based on a constant shortening rate and non-scaled Earth gravitational acceleration. The model reflected folding and doming of the lower ductile crust which is associated with the development of pop-ups and pop-downs in the upper crust. The scenario where the lower felsic crust is significantly less dense than upper part of the lower crust or middle crust (e.g. Lexa et al., 2011 or Maierová et al., 2012), and where gravitational inversion of such layers is induced, could not be involved in this approach due to problematics of the gravity scaling ($g_M = g_N$). However, we suggest that gravitationally driven diapiric exhumation is a native component of the processes associated to doming and uplift of the lower crust, including the molten component of the lower crust.

In this part the evolution of a crustal-scale Rayleigh-Taylor instability which is associated with inversion of a density stratified crustal segment of the lithosphere and with the diapiric exhumation of the weak felsic lower crust will be studied and discussed. The modelling follows the scheme presented in Krýza (2013) where parametric statistical study was employed and revealed that the density contrast (affected in time by radiogenic heat productivity) represents the most influential parameter which drives the rate and dynamics of crustal diapirism.

In this study we present new data that are complementary to Krýza (2013) and compare simulations that reflect various density contrasts, undulation of the interface of the basal layers and radiogenic heat productivity. Plotted strain(-rate) maps, material distributions, viscosity contrasts and GPE (gravitational potential energy) curves for selected simulations are discussed in the frame of the analogue models that are presented in *Chapter 3*. The model results are used to discuss the possibility of gravity driven uplift of the lower weak crust in frame of convergent models.

4.2 Model setup

The model domain represents a crustal-mantle segment ($150 \text{ km} \times 120 \text{ km}$, horizontal to vertical) that contains two, pre-defined material perturbations before crustal gravitational inversion (Fig. 41). The model domain is vertically stratified and individual layers represent the unified upper-middle crust (UC/MC), mafic lower

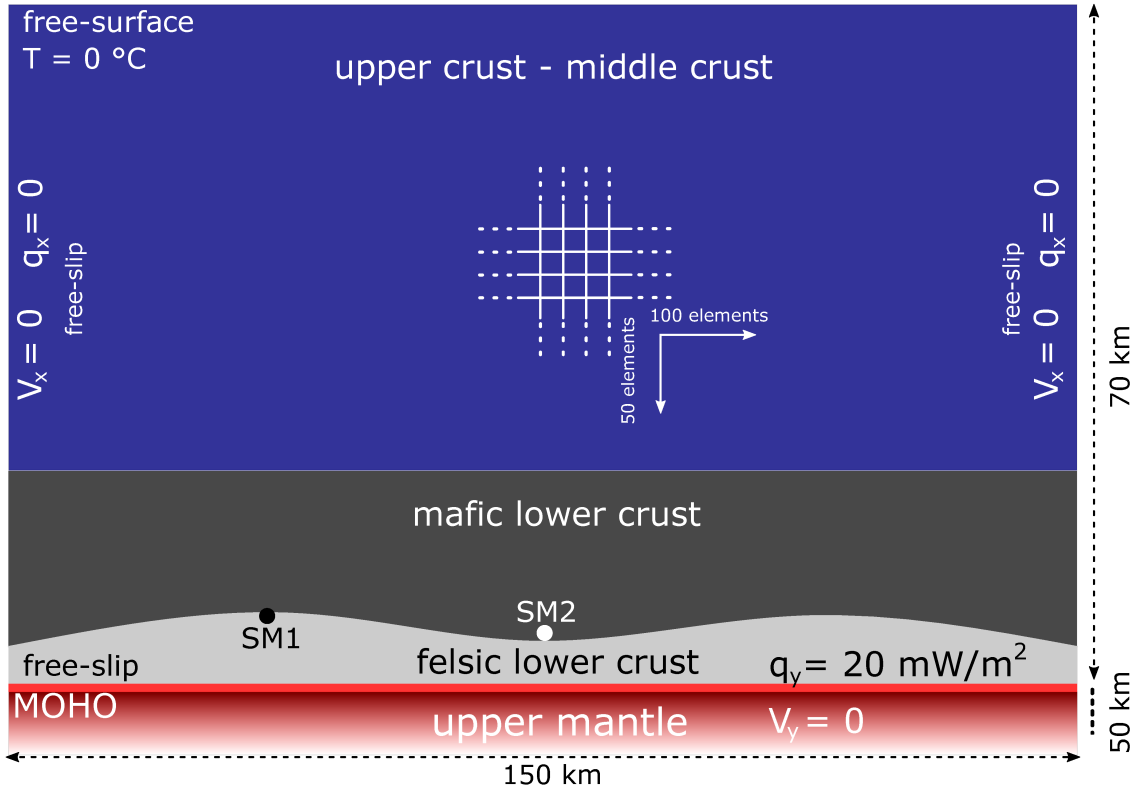


Fig. 41: Geometry and boundary conditions of the model domain. The upper boundary is deformable due to the free-surface b.c. and remeshing routine. For the top part is prescribed the Dirichlet b.c. with zero temperature. Both vertical boundaries are impermeable with prescribed free-slip b.c. in the vertical direction and zero heat flux in the horizontal direction. The base of the model is represented by the Neumann boundary condition with the heat flux in the vertical direction and with zero velocity in both directions. The MOHO line is represented by free-slip and represents the mechanical separation of the crustal and mantle segment. White points represent the special markers where the target output model parameters are traced.

crust (MLC), felsic lower crust (FLC) and upper mantle (UM). The UC/MC is defined as an initially colder, less dense segment with defined radiogenic heat productivity. The MLC represents the original high-density basement of a crustal segment which is stronger than the layer situated above and has no thermal productivity associated with radioactive decay. The FLC is a low-density and higher radiogenic heat productivity layer which represents a relaminant incorporated into the lithosphere during a convergent event (according to models of Maierová et al., 2012, 2016). The whole crustal segment is underlain by the upper part of the UM segment. This part does not play a significant role for mechanical evolution of the crustal segment in models with no longitudinal shortening but is important for heat transfer from the model base. In the presented model, and for each simulation, we do not consider this part as being mechanically coupled with the crustal segment. All model physical parameters all described in Fab. 9.

The model is set in a 2D domain (with Cartesian geometry) represented by numerical grid with resolution of 100 (horizontal) to 70 (vertical) bilinear quadrilateral (Q4) elements (size of individual element corresponds to 1.5 km to 1.7 km). The resolution of the crustal segment is 100 x 50 elements while the mantle segment has a resolution of a 100 × 20 elements (vertical spacing of elements in the mantle segment is progressively increasing from MOHO to model base while in the crustal segment the spacing is constant).

4.2.1 Governing equations

The model describes the complex deformation of a heterogeneous lithospheric environment related to heat flow between individual subdomains. The flow of incompressible material with neglected inertia is described by following equations (generally described for compressible solution in the section 1.6.2):

$$\begin{aligned}\nabla p - \nabla \cdot \sigma &= -\rho g e_z, \\ \nabla \cdot v &= 0,\end{aligned}\tag{4.1}$$

where ρ is the density, g is the gravitational acceleration, σ is the stress tensor, p is the pressure, v is the velocity and e_z is the unit vector in direction of z -axis. The equation follows the solution of the Stokes problem (e.g. Gerya, 2009). The heat transport in the model domain is represented by a prescribed heat transfer equation (following eq. 1.27 - subsection 1.6.3) with reduced source member to only radiogenic heat productivity H_r (other sources as latent, adiabatic or shear heating are neglected) as follows:

$$\rho c_p \frac{DT}{Dt} - \nabla \cdot \lambda(\nabla T) = H,\tag{4.2}$$

where c_p is the specific heat capacity under constant pressure, T is the temperature, t is the time, ρ is the density and λ is the thermal conductivity. In the model we assumed a non-diffusive evolution of the material composition on the geological time-scale:

$$\frac{Dc_i}{Dt} = 0, \quad \forall i > 0.\tag{4.3}$$

Density in our model is a function of the temperature and material composition:

$$\rho = \rho(T, \{c_i\}) = \rho_{\text{ref}}(\{c_i\}) [1 - \alpha(\{c_i\})(T - T_{\text{ref}})],\tag{4.4}$$

Tab. 9: The model parameters.

Physical parameters	Symbols	Values	Units
thermal conductivity	κ	2.5	$\text{Wm}^{-1}\text{K}^{-1}$
specific heat	c_p	800	$\text{Jkg}^{-1}\text{K}^{-1}$
gravitational acceleration	g	9.81	ms^{-2}
gass constant	R	8.314	$\text{JK}^{-1}\text{m}^{-3}$
mantle density	ρ	3300	kg m^{-3}
temperature at the surface of the model domain	T_p	273	K
heat flow at the base of the model domain	q_b	20	mW m^{-2}
switch-off of the thermal sources	T_f	1170	K
minimum and maximum viscosity (exp)	$\eta_{\min/\max}$	14 / 26	Pa s
referential values of plastic strain	$\epsilon_{0,\text{inf}}$	0 ; 1	
cohesion	C	1	Mpa
UC/MC - sediments, quarzit (Hirth et al., 2001; Ranalli, 1995):			
coefficient of thermal expansion	α	2e-5	
initial angle of internal friction	φ_0	15	°
finite angle of internal friction	φ_{inf}	7.5	°
viscosity exponent	n	3	
pre-exponential parameter	B	1.89e8	$\text{Pa s}^{1/n}$
activation energy	E_A	156	kJ mol^{-1}
referential density	ρ_0	2800	kg m^{-3}
radiogenic heat productivity	H_r	2e-6	$\mu\text{W m}^{-3}$
thickness	m	50	km
MMC - plagioklas (Ranalli, 1995):			
coefficient of thermal expansion	α	2e-5	
initial angle of internal friction	φ_0	30	°
finite angle of internal friction	φ_{inf}	15	°
viscosity exponent	n	3.2	
pre-exponential parameter	B	3.69e6	$\text{Pa s}^{1/n}$
activation energy	E_A	238	kJ mol^{-1}
referential density	ρ_{0A}	2950	kg m^{-3}
varied referential density (for various simulations)	ρ_{0B}	2800-3100	kg m^{-3}
radiogenic heat productivity	H	0	$\mu\text{W m}^{-3}$
thickness (varied from 5 to 15 km - according to FLC thickness)	m	5	km
FLC - granite (Ranalli, 1995):			
coefficient of thermal expansion	α	3e-5	
initial angle of internal friction	φ_0	30	°
finite angle of internal friction	φ_{inf}	15	°
viscosity exponent	n	1.9	
pre-exponential parameter	B	2.75e7	$\text{Pa s}^{1/n}$
activation energy	E_A	137	kJ mol^{-1}
referential density	ρ_{0A}	2750	kg m^{-3}
varied referential density (for various simulations)	ρ_{0B}	2650-2950	kg m^{-3}
radiogenic heat productivity (for various simulations)	H	2e-6 - 6e-6	$\mu\text{W m}^{-3}$
thickness (referential)	m	10	km
thickness (for various simulations)	m_A	5 - 15	km
undulation amplitude (referential)	A	3	km
undulation amplitude (for various simulations)	A_A	2 - 4	km

Tab. 10: The varied model parameters. Individual parameters are: amplitude of the interface undulation between MLC and FLC (A_F), thickness of the FLC, (Th_F), density of the MLC (D_M), density of the FLC (D_F) and radiogenic heat productivity of the FLC (H_F)

number of current value	A_F [km]	Th_F [km]	D_M [kg.m ⁻³]	D_F [kg.m ⁻³]	H_F [μ W.m ⁻³]
1	2	5	2800	2650	2
2	2.5	7.5	2875	2725	3
3	3	10	2950	2800	4
4	3.5	12.5	3025	2875	5
5	4	15	3100	2950	6

where ρ_{ref} is the referential density - which is chosen according to defined material (see Tab. 10), T_{ref} is a referential temperature - chosen always as 273 K and α is a heat expansion coefficient which depends on a given material.

Heat sources (radiogenic heat productivity H_r) are dependent on material composition:

$$H = H(\{c_i\}), \quad (4.5)$$

where non-zero values are initially prescribed for UC and FLC with variable initial values for FLC according to individual simulations.

The deviatoric stress tensor is a function of strain-rate, temperature, pressure and composition:

$$\begin{aligned} \sigma &= \sigma(\dot{\epsilon}, T, p, \{c_i\}) \\ \sigma &= \begin{pmatrix} \sigma_{xx} & \sigma_{xz} \\ \sigma_{zx} & \sigma_{zz} \end{pmatrix} e_x \otimes e_x + \begin{pmatrix} \sigma_{xz} & \sigma_{zx} \\ \sigma_{zz} & \sigma_{zz} \end{pmatrix} e_x \otimes e_z. \end{aligned} \quad (4.6)$$

In the whole model domain we prescribed a non-linear visco-plastic rheology affected by stress acting on crustal material. The plastic deformation in the UC also represents an approximation of a brittle failure which dominates in low T systems with high strain-rates while high T systems with low deformation rates are affected by viscous flow. The viscous flow is characterized by irreversible deformation of a material where the strain-rate depends on acting stress. The plastic deformation is also irreversible but is considered when differential stress yield limit is reached (σ_{yield}). This functional dependency of deviatoric stress (equation 4.6) is possible to express for visco-plastic regime by using the effective viscosity (η_{eff}) as:

$$\sigma = 2\eta_{\text{eff}}\dot{\epsilon}, \quad (4.7)$$

where $(\dot{\epsilon})$ represents the deviatoric strain-rate tensor (see section 3.3.5 and eq. 3.2). For a viscous regime (when the value of the second invariant of the deviatoric stress tensor is smaller than a yield stress ($\sigma_{II} < \sigma_{\text{yield}}$)) is a deformation represented by dislocation creep which is defined by non-linear relationship between stress tensor and strain-rate tensor. This could be expressed as:

$$\dot{\epsilon} = A \frac{3^{\frac{n+1}{2}}}{2} \sigma_{II}^{n-1} \exp\left(-\frac{E_A}{RT}\right) \sigma, \quad (4.8)$$

where R is the gas constant, $\sigma_{II} = \sqrt{1/2 \sigma : \sigma}$ is the second invariant of the deviatoric stress tensor, E_A is the activation energy, n is the power of the viscosity (stress invariant, respective) and A is the material constant. These parameters are experimentally stated (see Tab. 9; Hirth et al., 2001; Ranalli, 1995). Based on these relations, it is possible to derive the effective viscosity as follows (e.g. Maierová et al., 2012):

$$\eta_{\text{eff}} = B \dot{\epsilon}_{II}^{1/n-1} \exp\left(-\frac{E_A}{nRT}\right), \text{ where } B = \frac{1}{2} (A)^{-1/n} \frac{2^{(1-n)/n}}{3^{(n+1)/2n}}. \quad (4.9)$$

Here $\dot{\epsilon} = \sqrt{1/2 \dot{\epsilon} : \dot{\epsilon}}$ is the second invariant of the strain-rate tensor and B is the pre-exponential parameter. In the plastic regime is $\sigma_{II} = \sigma_{\text{yield}}$ (see subsection 1.3.1) and effective viscosity is derived from the equation 4.7 as follows:

$$\sigma_{\text{eff}} = \frac{\sigma_y}{\dot{\epsilon}_{II}}. \quad (4.10)$$

The yield stress for various materials is not constant but directly depends on some other parameters related to current material (such as porosity, grain size and grain distribution, chemical composition, temperature, pressure etc.). For rock behavior which is pressure-dependent we used *Drucker-Prager yield criterion* (according to Maierová et al., 2012):

$$\sigma_y = p \sin \phi + C \cos \phi, \quad (4.11)$$

where p is the pressure, C is the cohesion and ϕ is the internal friction angle. The parameters (B, E_A, n, ϕ, C) are dependent on the material composition ($\{c_i\}$) (see Tab. 9). The angle of internal friction ϕ depends on the plastic strain (defined as integration of the second invariant of the plastic strain-rate tensor - along trajectory

of the current material particle). This dependency is possible to express as follows (after Maierová et al., 2012):

$$\begin{aligned} \phi &= \phi_0 \quad \text{if } \varepsilon_{II} \leq \varepsilon_0, \\ \phi &= \phi_0 + (\phi_\infty - \phi_0) \frac{\varepsilon_{II} - \varepsilon_0}{\varepsilon_\infty - \varepsilon_0} \quad \text{if } \varepsilon_0 < \varepsilon_{II} < \varepsilon_\infty, \\ \phi &= \phi_\infty \quad \text{if } \varepsilon_{II} \geq \varepsilon_\infty, \end{aligned} \quad (4.12)$$

where ϕ_0 , ϕ_∞ , ε_0 and ε_∞ are parameters while ε_{II} is the integrated invariant of the plastic strain-rate.

For the evolution of the material composition the *particle-in-cell method* is used (Maierová et al., 2012; for the *marker-in-cell method* follow Gerya and Yuen (2003)). The principle of this technique is saving the information about material properties due to representative material markers (particles) that have supported advecting in the model domain by the velocity field. Each particle contains information about the material composition - which is not changed due to the time evolution - and about the commulated plastic deformation (represented by value of σ_{II}). The displacement of the particle is solved by fourth-order *Runge-Kutta method*. The material properties for every single particle in each timestep in each numerical grid element are evaluated at the integration points. In these points are calculated average values of a given material properties for all particles in current mesh element. In our model we followed the scheme of Maierová et al. (2012) where the effective viscosity is calculated from geometrical average as follows:

$$\log(\eta_{\text{eff}}) = \sum_i c_i \log(\eta_{\text{eff},i}), \quad (4.13)$$

while other quantities are calculated from arithmetic average as:

$$P = \sum_i c_i P_i, \quad (4.14)$$

where i denotes the component of the material and c_i is a fraction of this component in the calculation of the current quantity. During the computation of the c_i and $\varepsilon_{II,i}$ in current point which is given by coordinates x, z (for two-dimensional domain), we used the following relationship (Maierová et al. (2012) after Gerya and Yuen (2003)):

$$c_i = \frac{\sum_{n_i} w_{n_i}}{\sum_n w_n}, \quad \varepsilon_{II,i} = \frac{\sum_{n_i} \varepsilon_{II,n_i} w_{n_i}}{\sum_n w_{n_i}}, \quad (4.15)$$

where n_i represents the marker which corresponds to the current material, n is the index for summing over all markers for current mesh element and w_i is the weight for respective marker which is calculated as follows:

$$w_n = \frac{1}{\Delta x^{\max} \Delta z^{\max}} \left(1 - \frac{\Delta x_n}{\Delta x^{\max}} \right) \left(1 - \frac{\Delta z_n}{\Delta z^{\max}} \right), \quad (4.16)$$

where Δx_n and Δz_n are distances of the markers from point $\{x, z\}$ and Δx^{\max} and Δz^{\max} represents the maximum value of those distance for all markers in the current element.

4.2.2 Boundary conditions

At the boundaries of the model domain we imposed boundary conditions (b.c.) describing how the model is related to the potentially surrounding regions. The topography effect of the model surface and the mantle bulging are neglected (model has implemented free-surface boundary condition but the finite shape of the model surface does not affect the inner dynamics. Lateral deformation (shortening) of the domain is not included in the model setup.

For the top of the model we set a free-surface boundary condition without sedimentation/erosion factors which would not play a significant role in our model scenario (for incorporation of the sedimentation or erosion processes follow Maierová et al. (2012)). Both lateral boundaries and the bottom of the crustal segment have prescribed free-slip b.c. while side boundaries and bottom of the mantle segments have no-slip b.c. (mantle segment is in most of the simulations used only for heat transfer to the crustal segment). Thermal b.c. is set as *Dirichlet* b.c. for the model surface where $T = 0$ K while for model base is set *Neumann* b.c. where the heat flux is $q = 20$ mW/m². Both model sides are thermally isolated from outer regions, i.e. $q = 0$ mW/m².

4.2.3 Initial conditions

In the model we tested variations of the several input parameters as is described above. These parameters are set as: 1. amplitude of undulation of the interface between MLC and FLC ($A_F = 2 - 4$ km with step of 0.5 km); 2. thickness of the FLC (ratio of thickness of the FLC and MLC, respectively) which is related to the amount of radiogenic heating produced by the FLC ($Th_F = 5 - 15$ km with step of 2.5 km); 3. radiogenic heat productivity of a FLC ($H_F = 2 - 6$ μ Wm⁻³ with step of 1 μ Wm⁻³); 4. density of FLC ($D_F = 2650 - 2950$ kg.m⁻³ with step of 75 kg.m⁻³); 5. Density of MLC ($D_M = 2800 - 3100$ kg.m⁻³ with step of 75 kg.m⁻³). All parameters are shown in Tab. 9 and 10 (amplification of undulated interface between the MLC and FLC is represented by median value of sinus in the predefined boundary line position).

4.2.4 Numerical implementation

All of the simulations are considered under the same numerical approach where the system of partial differential equations is solved. For solution of above prescribed equations we used multiphysical open-source software *ELMER FEM* which is based on the principle of the finite element method. The structure of numerical calculations is following (including procedures implemented to extend applicability to geodynamical modelling (Maierová et al., 2012) such as markers initiation and integration of plastic deformation, free-surface b.c. etc.):

1. Initialization of a thermal field - stationary solution of the heat transfer equation ($-k\nabla T$ from Eq. 1.27)
2. Estimation of the time-step
3. Interpolation of the viscosity and marker density to an integration point in the current mesh element - solution of the Stoke's problem (Eq. 4.1)
4. Interpolation of thermal sources and density from current markers to integration points - non-stationary solution of the heat transfer equation (Eq. 4.2)
5. Calculation of the advection of the free-surface
6. Deformation of the numerical mesh
7. Advection of the markers in the model domain and integration of the plastic strain
8. Saving of the calculated values and export to *.vtk* data file
9. Return to point 2.

4.3 Results

In this part will be described the general evolution of the model domain reflecting the variation of the model parameters with variation of the prescribed initial conditions. For further analysis of the diapir development and vertical extrusion is used only the set of simulations which reflects extreme values of the chosen initial conditions such as the density contrast of the MLC/FLC, amplitude of the Rayleigh-Taylor instability (A_f), radiogenic heating (H_f) in the FLC and contrast of thickness of both lower crust layers. All combinations of the prescribed initial conditions, and associated output model parameters, will not be described in this study (for details follow Krýza (2013)).

4.3.1 The output model parameters

Two series of parameters, that describe both global and local material properties and physical conditions in the model domain, serve well as relevant indicator of model behaviour (Fig. 42). The global parameters are related to the global model quantities (e.g. temperature, bulk strain(-rate), bulk stress, gravitational potential energy (GPE), kinetic energy, characteristic time of the simulation, position/movement of the gravitational centre of specified material - such as gravity center of the FLC material, etc.). On the small-scale of the model domain it is possible to trace the local model parameters which describe changes in some specific model subdomain (Fig. 42b)(e.g. maximum/minimum temperature and pressure, maximum pressure and temperature differences, pressure and temperature differences respective to aimed areas, specific time related to this P-T parameters, elevations of the material element or pathes, etc). Except previous, it is also possible to use kinematic and geometric parameters (Fig. 42c) that could be related to changes in a surfaces curvature (such as tracing the evolution of a curvature along specific material boundary - e.g. curvature of a diapiric surface), particle movement described by the absolute and relative distances (e.g. tortuosity of a particle trajectory) and others.

Global output model parameters

The set of these parameters is based on investigation of gravitational potential GPE (Fig. 42d) evolution in the model domain through model evolution. The curve which represents the GPE is unique for each simulation and is characterized by a lower plateau, inflection and upper plateau that corresponds to the maximum GPE, higher dynamics during material inversion and minimum GPE of the system. The GPE is in the model represented by distribution of FLC material in current time-step which reflects progress in the material inversion. Initial state of the model is then represented by higher values of the GPE while finite state correlates with a minimum values. The GPE in each timestep is expressed as:

$$U = mgh, \quad (4.17)$$

and change of the GPE is expressed as:

$$\Delta U = mg\Delta h, \quad (4.18)$$

respective. Here $m = m^t(\rho_i)$ is the mass of the material element and U is calculated as the integral over the area related to the felsic material in each time-step. The mass is related to the density with dependence on t while h represents the vertical position of the material element with respect to the base of the crustal part of the model (MOHO). The GPE in each simulation is possible to substitute by calculation

of the gravitational center of the FLC material. The inflection of the curve which represents the vertical position of the FLC mass center in time corresponds to the most dynamic event of the model evolution - related to vertical extrusion (driven by density contrast of the FLC and MLC) of the felsic material. The individual global model output parameters are then related to:

- Inflection of the GPE curve (maximum dynamics of the system - maximum vertical extrusion rate)
- Difference between \sim maximum and \sim minimum of the GPE related to the lower and upper plateaus
- Corresponding time for both features described above

While the slope of the first part of the curve (part of which is represented by the distance from the beginning to the inflection) is typically reflecting the acceleration of the vertical extrusion, the upper plateau is defined as the site of higher deceleration of the extrusion (marked as *rp*). This threshold is defined as the time where the increment of the extrusion (negative increment of the GPE) is evaluated as smaller than the average value from the interval between inflection and finite time-step of the simulation.

The following set of parameters is based on the above described features of the GPE evolutionary curve (Fig. 42d):

1. D_max (the characteristic time of the maximum system dynamics - inflection of the GPE curve [Ma])
2. T_dom (average integral temperature of the model domain in D_max [K])
3. S_dom (average bulk strain-rate in the model domain in D_max [$\log \dot{\epsilon}$ [s⁻¹]])
4. dh (difference between the original position of the gravitational center of the FLC material and position of this gravity center in time of *rp* [km])
5. t_dh (corresponding time to dh [Ma])
6. H_max (maximum reached vertical position of the FLC material in the model domain - corresponds to *rp* position [km])

Local output model parameters

This set of the parameters is based on the P-T-t-d (pressure-temperature-time-space) conditions of the aimed markers in the model domain. The figure 42(a,b) displays strategy and position for special markers (SM or M) where target output parameters are calculated that are defined as:

1. T1_max (maximum reached temperature in the special marker SM1 [K])
2. P1_min (minimum reached pressure in the special marker SM1 [kbar])

3. T2_max (maximum reached temperature in the special marker SM2 [K])
4. P2_min (minimum reached pressure in the special marker SM2 [kbar])
5. h_t (specific time of between minimum and maximum depth reached by SM1 [Ma])
6. h_d (maximum vertical difference in the position of SM1 [km])
7. T_d (temperature difference corresponding to minimum and maximum elevation points of SM1 [K])

All the analyzed global model output parameters are sorted in the table 11. The correlation analysis and principal component analysis (PCA) of all input and output model parameters is possible to find in Krýza (2013). In the following text, the analysis will be restricted to qualitative comparison of the target parameters and description of thermal and mechanical features of the developed diapiric structure.

4.3.2 Initial thermal field and geotherm

A steady-state thermal field is generated during the first time-step by solution of the *Poisson* (conduction) equation and reflects well a laterally isotropic thermal field which has the same characteristic vertical gradient along this lateral direction (Fig. 43). The thermal field in this first time-step does not reflect the prescribed geometry of the upper-middle-lower crust. This is due to the time-dependent rheology and thermal parameters (such as radiogenic productivity) that are related to the model evolution after time-step 1. The thermal field corresponds to the conditions in massively thickened orogenic root before erosion which typically removes the upper crust (thickening, erosion and sedimentation are typically reflected by isostatic compensation). However, the erosion/sedimentation factor and the isostatic response are not prescribed in our model.

4.3.3 Evolutionary stages and the main simulation differences

The different evolutions which reflects the effect of individually prescribed initial conditions (Tab. 10) for each simulation can be divided into the three basic classes of the evolutionary trends (Fig. 44): 1. Gravitationally driven inversion of the lower crust which is associated with the diapiric exhumation of the FLC through the middle(-upper) crust; 2. Gravitationally driven inversion of the FLC and MLC with the stabilisation of the FLC at the level of the originally positioned MLC; 3. Gravitationally driven collapse and stabilisation-equilibration of the felsic lower crust along the MOHO level.

For further reading, the notation of various simulations will be introduced here. All variations in the initial parameters are numbered after labeling of an appropriate parameter (e.g. D_{M1} corresponds to the first value of the density of the MLC

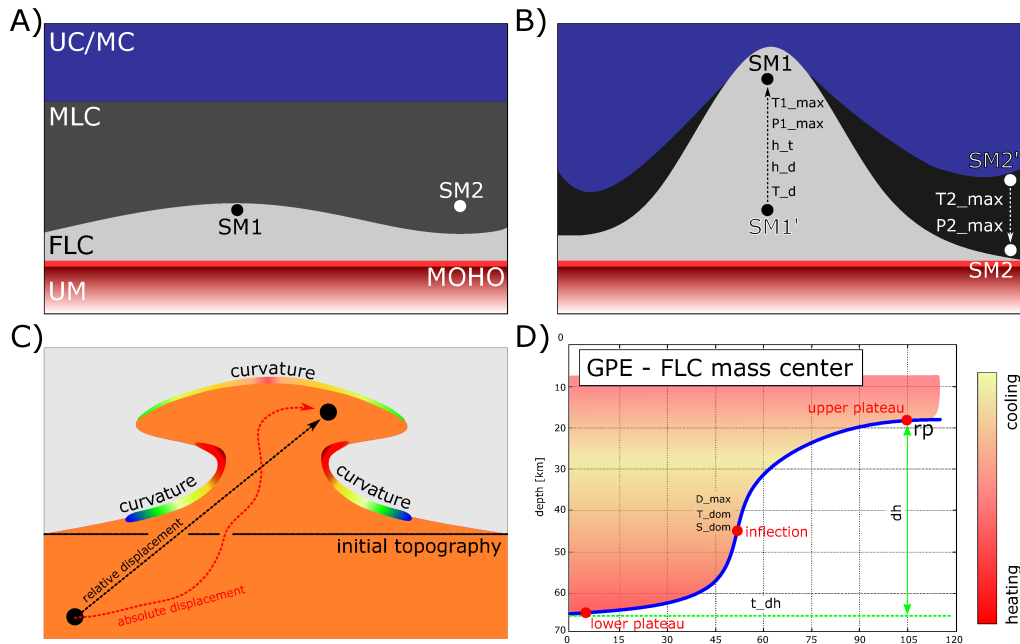


Fig. 42: Model output parameters. In the panels (a,b) are shown positions of the special markers where the local model output parameters are traced inside the model domain (for resultant values see Tab. 11). Panel (c) shows example of the strategy chosen for selection of the global output model parameters. The chosen model output parameters are related to the time-evolution of the gravitational potential energy (GPE) in the model domain. The GPE is related to the position of the felsic material mass center in the model domain in current time-step. This curve is associated with the minimum, maximum and inflection of the evolutionary trend (d). The inflection point reflects the time-step where the model dynamics is at the highest (maximum kinetic energy of FLC mass center - also derived from FLC material particles) while the high plateau of this curve represents a convergence of the GPE to a stable state. The difference between lower and upper plateau of the GPE curve represents the specific time for the vertical extrusion of the FLC material. All parameters derived from this GPE evolution and related to curve target point are described in the text.